8-27-2012

Oblique shock interactions with gas cylinder interfaces

Ross White

Ross Liam White
Candidate

Mechanical Engineering
Department

This thesis is approved, and it is acceptable in quality and form for publication:

Approved by the Thesis Committee:

Peter Vorobieff , Chairperson

Sanjay Kumar

Svetlana Poroseva

C. Randall Truman

Oblique Shock Wave Interactions With Gas Cylinder Interfaces

by

Ross L. White

B.S., Mechanical Engineering, University of New Mexico, 2010

THESIS

Submitted in Partial Fulfillment of the
Requirements for the Degree of

Master of Science
Mechanical Engineering

The University of New Mexico

Albuquerque, New Mexico

July, 2012

Dedication

To my family, for putting up with me all these years.

Acknowledgments

First of all, I would like to thank Dr. Peter Vorobieff for taking me on this project and allowing me to blow things up at work. I would be already cranking away at a 9-5er if it were not for this opportunity. I would also like to thank Dr. Randall Truman and Dr. Sanjay Kumar for answering my handfuls of naive questions about fluid dynamics with calm and a pinch of humor. Special thanks to Dr. Michael Anderson for his teachings in batch file processing and his numerical approach/outlook on experimental processes. Thanks to my colleagues Joseph Conroy and Patrick Wayne for the countless hours of work in the shock tube facility and post-processing all of our data. This work was funded by US National Nuclear Security Agency (NNSA) under the Stewardship Science Academic Alliances program through DOE Grant DE-PS52-08NA28920 and by the US Defense Threat Reduction Agency (DTRA) under awards HDTRA1-07-1-0036 and HDTRA1-08-1-0053. Without this funding, none of this work could have been performed.

Oblique Shock Wave Interactions With Gas Cylinder Interfaces

by

Ross L. White

B.S., Mechanical Engineering, University of New Mexico, 2010

M.S., Mechanical Engineering, University of New Mexico, 2012

Abstract

This thesis presents an experimental study of fluid instabilities formed due to an oblique interatction of a shock wave with a cylindrical gas column seeded with glycol droplets. Two gases are injected into quiescent air to form the column. The first is sulfur hexafluoride (SF_6) which generates the well-known Richtmyer-Meshkov Instability (RMI) when impulsively accelerated by a shock wave. This instability is formed due to the misalignment of the pressure and density gradients during the acceleration phase. The second is air. In this case, there is no macroscopic density gradient between the gas column and the surrounding air. Nonetheless, an instability similar to RMI develops due to the presence of the glycol droplets. Experimental studies are performed at an oblique angle of 15° and a Mach number of 1.67. Experiments of this nature typically make an assumption that the cylindrical gas column is nominally two-dimensional to simplify the problem. The validity of this assumption is explored by investigating the morphology of the instabilities in multiple horizontal planes and a vertical plane. Major variations of the morphology only occur near

the bounding walls, with less variation far from these walls. An investigation of the rotation of the gas column is also presented.

Contents

List of Figures

Chapter 1

Introduction

The Richtmyer-Meshkov instability (RMI) is a hydrodynamic instability that is generated when an interface between two fluids of differing densities is impulsively accelerated. The instability develops due to a misalignment of the density and pressure gradients which results in the deposition of vorticity on the interface, causing any initial perturbation of the interface to grow with time and eventually transitions to fully turbulent flow.

Recently, it has been shown experimentally [1] and numerically [2, 3] that there exists a class of instabilities that are analogous to RMI. This class of instabilities can develop in multi-phase flows, where the average density gradient is caused by a second, non-fluid phase [2]. Here, the vorticity is generated via a different mechanism, namely momentum exchange. In the case of impulsive (shock) acceleration, the particles initially lag behind the shock-accelerated gas, exchanging momentum with it and thus slowing it down. This leads to a different equilibrium velocity for the seeded volume, and to shear between the seeded and unseeded gas. This shear generates vortex roll-up on the *average* density interface. A discussion of the history of this class of instabilities will be presented followed by a description of numerous

studies and experiments regarding RMI.

1.1 History

The study of what happens at an interface between two fluids has long been a subject of great interest in the world of fluid dynamics and has led to discoveries of many well-known instabilities. Perhaps the most well-known of this type of instability is the Kelvin-Helmholtz instability (KHI). KHI was first discussed in 1868 by Hermann von Helmholtz [4], and by Lord Kelvin in 1871 [5]. KHI occurs when there is a significant velocity difference across the interface between two fluids (usually of the *same* density) resulting in the manifestation of vortices at the interface. When the velocity difference is large enough, these vortices can have enough energy to become unstable, leading to turbulence. Examples of KHI have been observed in clouds, the Sun's corona, Saturn's bands, just to name a few [6]. Another well-known instability is the Rayleigh-Taylor instability (RTI) first discussed by Lord Rayleigh in 1883 [7]. RTI is an instability which occurs at the interface between two *immiscible* fluids of differing densities that have a constant acceleration imposed on their interface. Lord Rayleigh considered the case of a heavy fluid layer suspended over a lighter fluid layer and both being subject to Earth's gravitational acceleration. The interface between the two immiscible fluids was initially almost planar. As the heavier fluid moves downward the lighter fluid is forced upwards in a "finger-like" pattern. These fingers develop due to growth of initial perturbations or disturbances at the interface. In 1950, G.I. Taylor noted that this same phenomenon will occur if the fluids are subjected to an artificial acceleration in which the lighter fluid is forced into the heavier fluid [8]. A modification of Taylor's theory led to Richtmyer's prediction of the Richtmyer-Meshkov instability (RMI). RMI occurs when an interface between two fluids of differing densities are *impulsively* accelerated and is therefore considered

to be the impulsively-accelerated limit of RTI. RMI was first discussed by R.D. Richtmyer in 1960 [9] and later verified experimentally by E.E. Meshkov in 1969 [10]. Richtmyer's approach was to consider an inviscid, essentially incompressible system, in which a sharp and well-defined interface between two fluids is subjected to an acceleration profile in the form of a delta function. Then a hydrodynamic instability that develops due to misalignment of the pressure and density gradients. This misalignment generates vorticity through the baroclinic term in the vorticity equation, as seen in Equation 1.1 [14].

$$\frac{D\vec{\omega}}{Dt} = \vec{\omega} \cdot \vec{\nabla}\vec{u} + \vec{v}\vec{\nabla}^2\vec{\omega} + (\frac{1}{\rho^2}\vec{\nabla}\rho \times \vec{\nabla}p)_{Baroclinic\ Term} \tag{1.1}$$

The amount of vorticity deposited depends on the strength of the pressure and density gradients. The strength of the pressure gradient is essentially measured as the strength of the impulsive acceleration. In the case of a shock wave acting as the impulsive accelerator, this depends upon the Mach number, $M = v/c$, where v is the velocity of the shock front and c is the speed of sound in the medium. For the strength of the density gradient, the Atwood number, defined in Equation 1.2, is used. Typically, ρ_2 is larger than ρ_1.

$$A = \frac{\rho_2 - \rho_1}{\rho_2 + \rho_1} \tag{1.2}$$

The development of RMI begins with small amplitude perturbations that initially grow linearly with time, in accordance with "Richtmyer's linear stability theory". This is followed by a non-linear regime where a "bubble-spike" character of instability becomes visible, with "spikes" of heavier fluid falling into lighter fluid and "bubbles" of lighter fluid rising into heavier fluid. Eventually, the instability transitions to turbulence, due in part to the development of KHI at the interface, mixing the two fluids together. In RTI, the perturbations grow exponentially with time when the amplitude is sufficiently smal. RTI only occurs when the light fluid accelerates a heavy fluid. In RMI, on the other hand, the instability grows at a nearly constant rate during early times and develops regardless of the orientation of the imposed

acceleration, i.e. heavy to light and vice versa [11]. RMI can be observed in a variety of problems ranging from Inertial Confinement Fusion (ICF) [12] to Super Nova Remnant (SNR) formation [13]. For the work presented in this thesis, RMI is of utmost importance.

1.2 Governing Equations

To describe the behavior of a shock wave, both before and after the shock passage, the following equations will be used. These are the *standing normal shock* wave governing equations for a perfect gas [14]:

$$\frac{p_1 M_1}{\sqrt{T_1}} = \frac{p_2 M_2}{\sqrt{T_2}} \tag{1.3}$$

$$T_1(1 + \frac{\gamma - 1}{2} M_1^2) = T_2(1 + \frac{\gamma - 1}{2} M_2^2) \tag{1.4}$$

$$p_1(1 + \gamma M_1^2) = p_2(1 + \gamma M_2^2) \tag{1.5}$$

where γ is the specific heat ratio, and p_1, M_1, T_1, p_2, M_2, T_2 are the state variables of pressure, Mach number, and temperature, corresponding to before and after the shock wave has passed, respectively. Given a state before the shock arrival defines p_1, M_1, T_1 and hence, Equations 1.3, 1.4, 1.5 are sufficient to calculate the state after the passage of the shock. Useful transformations can be made to the above equations. Equation 1.5 can be solved for the pressure ratio [14]:

$$\frac{p_2}{p_1} = \frac{1 + \gamma M_1^2}{1 + \gamma M_2^2} \tag{1.6}$$

The post shock Mach number M_2 can be shown to be:

$$M_2^2 = \frac{M_1^2 + \frac{2}{\gamma - 1}}{\frac{2\gamma}{\gamma - 1} M_1^2 - 1} \tag{1.7}$$

Notice the dependence on only M_1 and γ. Plugging Equation 1.6 into Equation 1.7 simplifies the dependence of the pressure ratio and can be reduced to:

$$\frac{p_2}{p_1} = \frac{2\gamma}{\gamma+1}M_1^2 - \frac{\gamma-1}{\gamma+1} \tag{1.8}$$

A similar procedure can be performed on Equation 1.4, yielding the temperature ratio to be:

$$\frac{T_2}{T_1} = \frac{(1+[\frac{(\gamma-1)}{2}]M_1^2)([\frac{2\gamma}{(\gamma-1)}]M_1^2-1)}{\frac{\gamma+1}{2(\gamma-1)}M_1^2} \tag{1.9}$$

Equation 1.9 shows that the system will undergo a temperature increase. Combining Equations 1.8 and 1.9 forms the density ratio [14]:

$$\frac{\rho_2}{\rho_1} = \frac{(\gamma+1)M_1^2}{(\gamma-1)M_1^2+2} \tag{1.10}$$

The density ratio is a direct result of gas compression and tends to a constant limit. For a monatomic gas, this limit is $\rho_2 = 4\rho_1$ [14].

The equations listed above are the governing equations for a standing normal shock wave and are therefore assumed applicable only to perfect gases. In our experiments, however, the injection of a Sulfur-Hexafluoride, SF_6, gas cylinder seeded with glycol droplets presents a two-fold problem. Firstly, after the passage of the shock, the particles themselves lag behind the flow and affect the flow characteristics [1, 15, 16]. Secondly, after the particles catch-up, they continue to affect the flow structure [17]. There are many applications where the dispersion of particles in turbulent shear flows are a concern, such as the injection of gasoline in an internal combustion engine. Understanding the influence of the particles on the flow structure, especially in the transition to turbulence regime, is therefore of great importance.

Elghobashi [17] realized that the prediction of these transport phenomena requires knowledge of the two-way nonlinear coupling between the particles and turbulence,

i.e. the response of the discrete particles to the turbulent motion of the fluid, and the effect of the particles motion on the frequency spectrum of turbulence [17]. He used a direct numerical simulation (DNS) method to predict the behavior of these turbulent flows laden with particles. According to his analysis, several quantities are required to define the character of the effects that the particles will have on the flow. These include particle size, spacing between particles, and concentration. It was shown that these will have different effects on the flow. To designate the interaction between the particles and turbulence, the terms "one-way coupling", "two-way coupling", and "four-way coupling" were used. In "one-way coupling", the particle dispersion depends on the state of turbulence but there is no feedback to the turbulence itself. In two-way coupling the particle loading (aka concentration) is large enough to alter the turbulent structure. Here, there is an increased dissipation rate of turbulent energy as the diameter of the particles decrease for the same particle material and fluid viscosity. Elghobashi notes that as the particle response time increases for a given particle concentration, the particle Reynolds number increases and vortex shedding takes place resulting in enhanced production of turbulent energy [17]. In "four-way coupling" the particle concentration is large enough that there are actually particle/particle collisions taking place. Due to this magnitude of particle concentration in these types of flows, they are sometimes referred to as "dense suspensions" [17]. Flows in the "one-way" and "two-way" coupling regimes are commonly referred to as "dilute suspensions" and because they are much less complex, most studies are confined to these regimes [17]. Direct numerical simulations (DNS) provide modeling-free, three-dimensional, instantaneous velocity fields for fluids in simple turbulent flows. These fields can be used to calculate the three-dimensional trajectory of a particle from which the dispersion statistics can be obtained [17]. The conclusion of this work shows that depending on the particle characteristics, mass loading/concentration in the flow, and the carrier fluid, particles can in fact alter the turbulent structure in shear flows. A discussion of the type of coupling we observe

and of the effects of particle size will be presented in the following sections..

1.3 Goals of Study

The work presented in this thesis is in support of recent numerical work done regarding oblique shock wave interactions with gas column cylinders [2], specifically, experimental validation of the simulations presented. Experimental validation of numerical simulations is extremely important in fluid mechanics and is an integral part to understanding the methods in which fluid instabilities develop temporally and spatially. Some of the numerical observations by Anderson [2] and McFarland et al. [18] had not yet been validated experimentally. Our work elucidates these observations and attempts to draw some conclusions regarding the mechanisms involved.

Many experiments and simulations have been done that are relevant to our work. In the following sections, a discussion of the earlier oblique shock/interface interaction will be presented, followed by the most recent experimental studies involving a seeded gas column. Both the experiments and their relationship to modeling will be discussed.

Chapter 2

Earlier Work on the Richtmyer-Meshkov Instability

The study of RMI has mainly been confined to the interaction of a shock wave moving in a direction normal to the plane (or axis) of a density interface and the according development/evolution of this phenomenon. Over the past twenty years, however, the interaction of an oblique shock wave with a density-stratified interface and the development/evolution thereafter have become the focus of many investigations, until recently only numerical [2, 12, 19, 23]. Experimentally, this type of RMI has been studied mainly using shock tubes [11, 16, 25]. The experiments in this thesis are therefore performed in a shock tube environment and will be discussed in detail in following chapters.

2.1 Oblique Shock Wave Studies

In the early 1990s, many contributions were made to this field. Yang et al. [19] laid the groundwork for the modeling shock-driven vortex flows. They characterized

the physical system by a shock wave propagating through a fluid of density ρ_1, impacting an interface, and proceeding through a region of density ρ_2 [19]. They used the density ratio $\eta = \rho_1/\rho_2$ for a simple quantification of the difference between the two fluids. This parameter divided the potential experiments/models into two distinct categories: one in which the shock crosses into a fluid with a higher sound speed, $\eta < 1$, also known as the "slow-fast" of s/f interaction, and one in which the shock crosses into a fluid with a lower sound speed, i.e. $\eta > 1$, known as the "fast-slow" or f/s interaction. They noted that this designation in terms of sound speed or wave impedance was physically meaningful [20]. Here I will only discuss the f/s interaction as it is directly related to the experiments of this thesis.

Richtmyer [9] considered the linear response of an impulsively accelerated, sinusoidally perturbed interface in which the shock propagates from a light fluid into a heavy fluid, i.e. the s/f case. His linear stability theory was shown to have good correlation with the experiments of Meshkov [10] at early times. The analysis of Yang et al. [19] also concludes that the s/f interaction will be "stable" and the f/s interaction will be "unstable", which can be misleading: interfacial perturbations would grow in both cases. Analytical efforts are typically confined to early time events and small/infinitesimal perturbations, the regime in which linearity can be exploited [19]. Beyond this regime, however, both the s/f and f/s interfaces depart strongly from their initial configurations [19], developing into increasingly distorted (unstable) surfaces. Because of this constraint, an alternative "vortex paradigm" was proposed in which the evolving interface yields coherent vortex structures, the essential components for understanding turbulent mixing at the interface [21]. To model the experiments of an oblique shock wave interaction with a density-stratified interface, Yang et al. [19] employed the conservative form of Euler's equations in two dimensions, namely the mass, momentum, and energy conservation equations for an inviscid, compressible fluid. To simulate a two-dimensional cross-section of a three-dimensional space, they used Cartesian coordinates as shown in Figure 2.1,

top. The shock moves from left to right and the interface is initially inclined to an angle, θ_0, where the two fluids are initially in pressure equilibrium, i.e. $p_1 = p_2$ [19]. The initial discontinuous interface is approximated by a linear interpolation of the density using a fractional distance, as seen in Figure 2.1 [19]. The upper and lower boundaries are modeled as perfectly reflecting walls, i.e. $v \cdot n = 0$, introducing mirror symmetry. The left and right boundaries are modeled as inflow/outflow boundaries, respectively, allowing mass transfer in and out of the model. The essential parameters of their model were the density ratio $\eta = \rho_1/\rho_2$ (as mentioned earlier), the Mach number M of the incoming shock, and the initial offset angle of the interface θ_0. For the simulation, Yang et al. used a second-order Godunov scheme of the type described by Colella and Woodward [22]. The results of the $M = 1.2$, $\theta_0 = 30°$, and $\eta = 3.0$ case, i.e. an f/s case, are shown in Fig 2.1, bottom:

Figure 2.1, bottom, displays images in a time sequence of density, pressure, and vorticity, in the left, upper-center, and right columns respectively. The rows correspond to the numbers in the caption and the top most row is just as the shock has nearly passed the interface. It is seen that negative vorticity is being deposited along the interface, where the sign of the vorticity is determined by the fact that the velocity "above" the interface is larger than that of "below" the interface. The interface maintains its straightness for some time after the shock has passed, except for the upper and lower boundaries where vortex roll-up and "binding" have occurred. The term "binding" is used to describe the pairing of opposite-signed vorticity regions into a coherent structure, in this case the wall vortex and its image [19]. The vortex binding actually stretches the interface, increasing the amplitude of the initial sawtooth perturbation. At late times it is evident that there is a breaking of symmetry due to the interaction of the interface with the following two positive weak vortex sheets: one at the lower boundary, the other at the upper boundary. The vortex sheets are, respectively, generated by the bent transmitted and bent reflected shocks [19]. These shocks produce a reflected shock that interacts with the interface, how-

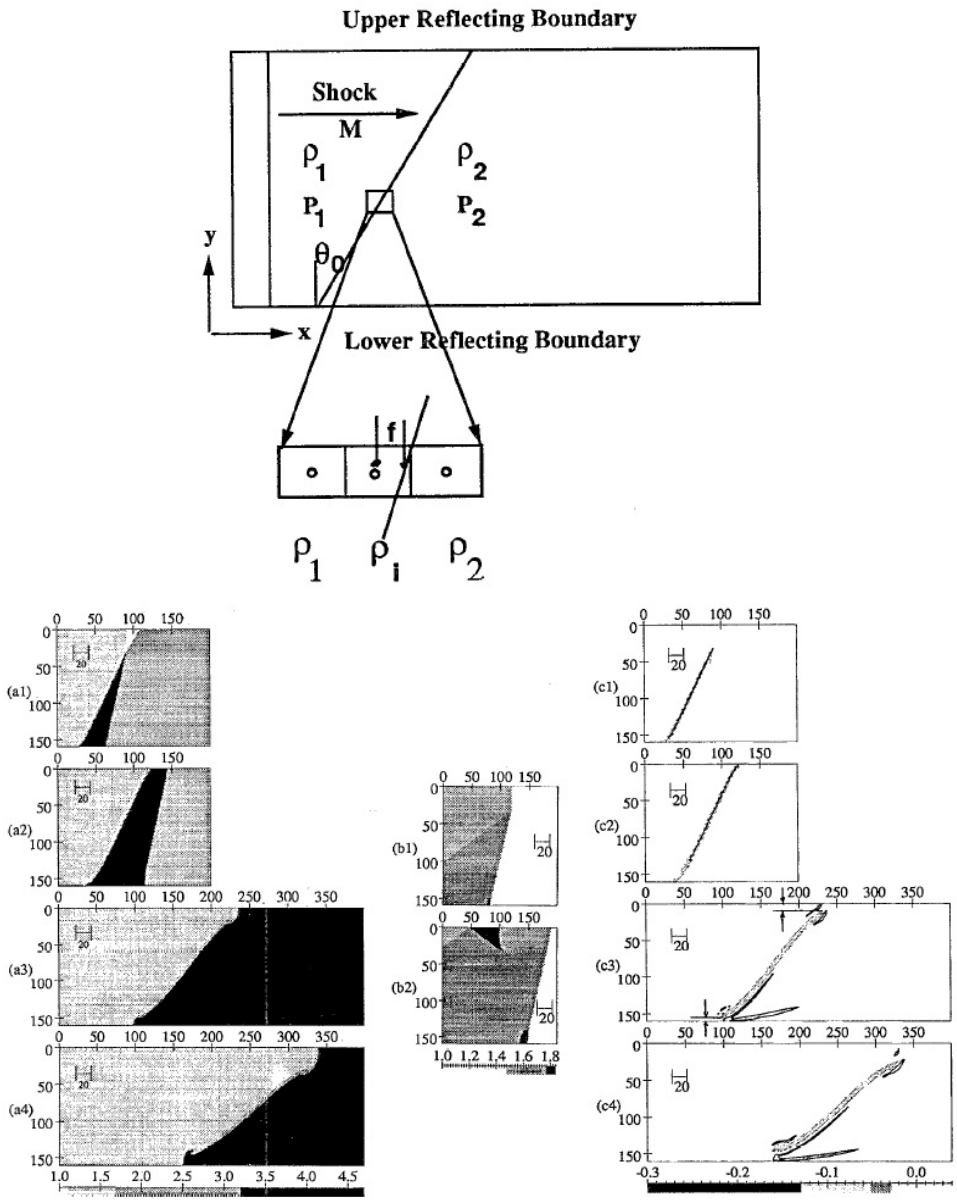

Figure 2.1: Top: Schematic of the computational domain, initial and boundary conditions. Bottom: Images for a M=1.2 shock interacting with a f/s interface. Presented in a time sequence: density, (a1)-(a4) left column; pressure, (b1) and (b2), center column; and vorticity, (c1)-(c4), right column. The times for these images are row 1, t=13.83 (100); row 2, t=27.50 (200); row 3, t=109.05 (800); and row 4, t=192.15 (1400) [19].

ever, these baroclinic effects were relatively weak [19]. The stretching of the interface acts to stabilize the shear layer inherent in the flow interface. If the strength of the shear layer is large enough, vortical rollers will develop along the interface as a result of the non-linear growth of the aforementioned Kelvin-Helmholtz (KH) instability [5]. Yang et al. [19] also performed a measurement of the total circulation of the interface. The changes in the slopes of the circulations are due to the influence of the many post-shock reflections and secondary shock-interface interactions.

Yang et al. [19] considered the shock interaction of this system as a "regular refraction", meaning that all three of the waves (the incident, reflected, and transmitted) and the rotated interface were locally planar and met at a single node on the interface. Because of this, they were able to use local Shock-Polar Analysis (SPA) to calculate the location of domain boundaries (angles) and variables in these domains including the local velocity jump across the counterclockwise-rotating interface. They then quantified the circulation at an f/s interface by comparing SPA and diagnostics of numerical simulations. Shortly after this contribution, Samtaney and Zabusky presented analytical expressions for circulation at f/s planar gas interfaces using SPA. They used this to analytically predict the circulation on non-planar interfaces. Figure 2.2 shows the different interface schematics they used. The physical situation they used is identical to the one Yang et al. [19] used: i.e. a shock propagating through a medium of density ρ_1, across an interface, and passing through into a region of density ρ_2. Three possible situations were presented as shown in Figure 2.2: a) planar interface inclined at an angle α; b) a sinusoidally perturbed vertical interface with amplitude, A, and wave length λ; and c) a bubble of radius r_0. In addition, the parameters used to describe the situation were nearly identical, i.e. the flow depends on the Mach number, M, the density ratio, and the geometry of the density. The only difference in this case is the definition of the density interface: described by either α, A/λ, or r_0. Through some tedious mathematical manipulations, equations for the normalized circulation per unit length for SPA and for the

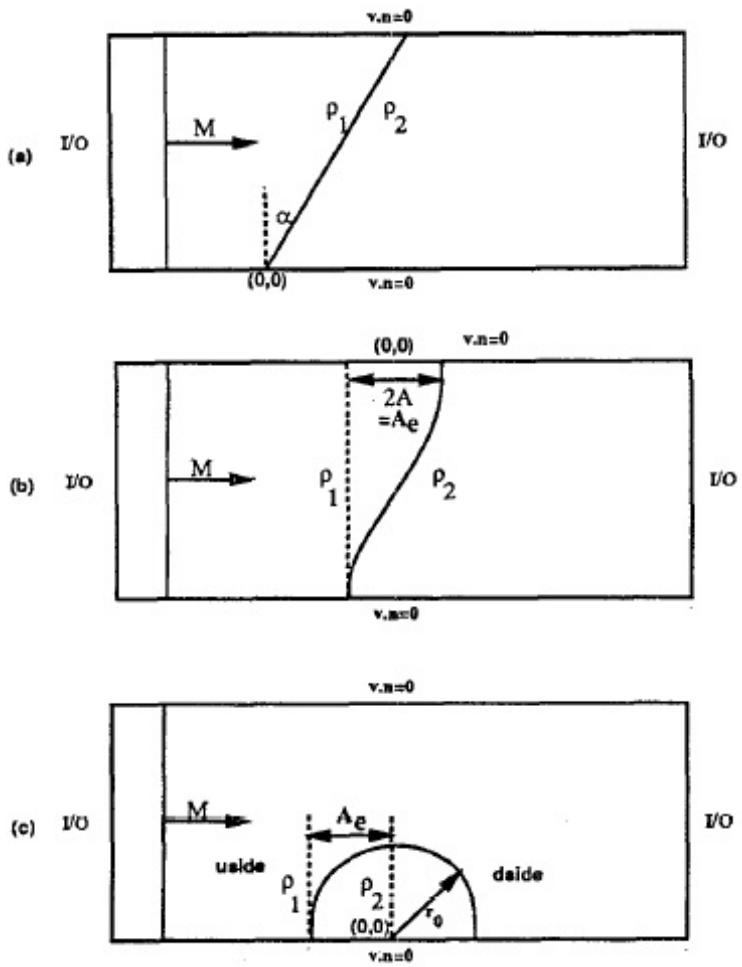

Figure 2.2: Schematic of physical domain and parameters in shock accelerated density stratified interfaces. (a) Planar interface; (b) sinusoidally perturbed inerface; and (c) circular interface [23].

approximation can be attained.

It is observed that the SPA result terminates at a certain critical angle while the approximate result can be extended to $\alpha = \pi/2$. This three-fold comparison shows excellent agreement up to moderate α, but at large α, the agreement is better for moderate to large Mach number [23]. They noted that a major source of error arose from comparing the SPA vortex sheet results with an evolving vortex layer that spreads because of numerical diffusion, hence, for larger α, the error is expected to be larger. Similar mathematical manipulations allow for the same comparison to be made for the sinusoidally perturbed and circular bubble interfaces.

For small A/λ ratios, a very good agreement between the analytical predictions and the numerical simulations was observed. Samtaney and Zabusky show where changes in γ, the ratio of specific heats, across the interface do not significantly affect the circulation [23]. Additionally, they used analytical expressions to develop models to predict the vorticity deposition in shock-bubble interactions and for the s/f (slow-fast) interfaces. For the sinusoidally perturbed interfaces, they used the expression for circulation and relate it to the growth rate of perturbations in the RMI environment [23].

In 2011, McFarland et al. [18] performed a computational study of the RMI for an inclined interface. A new shock-tube is being built currently and their study is the groundwork for the experiments to come in the near future. The computation was performed using a staggered mesh arbitrary Lagrange Eulerian (ALE) hydrodynamics code developed at Lawrence Livermore National Laboratory. A schematic of a section of the computational domain is shown in Figure 2.3, top.

In the simulations reported, McFarland et al. used a two-dimensional fixed Eulerian mesh at all times [18]. Their model included boundary layers of a simple functional form for the viscosity, imposed as solid, no-slip, insulated walls [18]. The

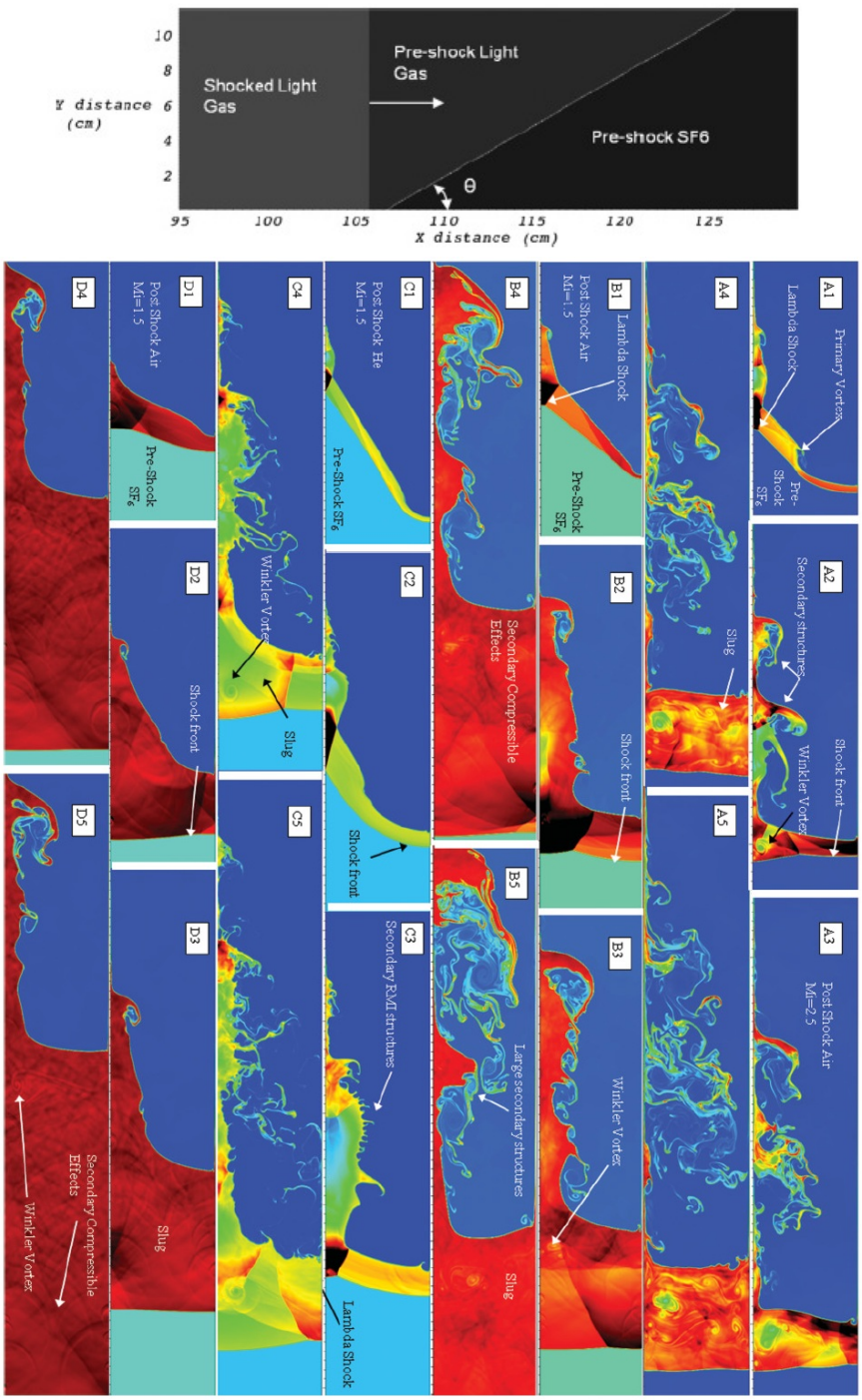

Figure 2.3: Top: Density plot of the initial conditions for an interface inclination angle of 30°. Bottom: (Color) Time series plot of density for three different parameter sets. Panels A1-A5, case 7, at times 0.5, 1.0, 1.5, 2.0, and 2.5 ms, respectively. Panels B1-B5, case 1, at times 0.5, 1.5, 2.5, 4.0, 5.5 ms. Panels C1-C5, case 13, at times 0.25, 0.5, 1.0, 1.5, 2.0 ms. Panels D1-D5, case 3, at times 0.5, 1.5, 2.5, 4.0, and 5.5 ms [18].

parameters of interest in the studies were the Mach number, the interface angle θ, and the Atwood number. They performed computations for 15 combinations of those parameters. A time series of density plots for four of the computations, i.e. using different parameter sets, is shown in Figure 2.3, bottom. In the figure, "case 1" refers to the combination of $M = 1.5$, $\theta = 30°$, and an $Air - SF_6$ gas pair; "case 3" refers to the combination of $M = 1.5$, $\theta = 60°$, and an $Air - SF_6$ gas pair; "case 7" refers to the combination of $M = 2.5$, $\theta = 30°$, and an $Air - SF_6$ gas pair; "case 13" refers to the combination of $M = 1.5$, $\theta = 30°$, and an $He - SF_6$ gas pair [18].

All of the flows presented, qualitatively speaking, develop through the following stages. The incident shock wave impacts the inclined interface and produces a reflected and transmitted shock wave. The reflected/transmitted shock wave reflects off the upper/lower shock tube wall, interacting with the interface a second time. A region of SF_6 with low mixing evolves behind the transmitted shock front [18]. The transmitted shock then replanarizes and the low-mixing region becomes rectangular in shape, which can be seen most clearly in A4 of Figure 2.3. They refer to this region as the "slug" due to its rectangular shape [18].

The four combinations they used in Figure 2.3 allowed them to compare the effects of different parameters on the flow development. To establish a base, they used the development of case 1, which is characterized by large mixing area and slug, (parameter set B, Figure 2.3), to compare with the other three cases. Here, a strong λ-shock wave (Figure 2.3, B1), was formed and traveled up the slug until it impacted and reflected of the upper wall. Upon interacting with the interface after this reflection, many more secondary compressible effects of moderate strength resonated within the slug (Figure 2.3, B4). They noted that a weak Winkler-type vortex structure [18], is also formed within the slug (Figure 2.3, B3). As the flow progresses in time, the mixing region continues to develop and separates into two large secondary vortical structures of SF_6 that persist into late times (Figure 2.3,

B5) [18].

The effects of incident shock wave Mach number can be examined by comparing case 1 (Figure 2.3, set B) with case 7 (Figure 2.3, set A). The stronger incident shock wave in case 7 led to a higher degree of separation between the mixing region and the slug [18], which resulted in the early destruction of the λ-shock and allowing for the primary transmitted shock to replanarize quickly. This suppressed the secondary compressible effects within the slug that are seen in case 1 [18]. Also, a strong Winkler-type vortex structure was created within the slug that was joined by other smaller vortical structures at later times (Figure 2.3, A5).

Atwood number effects were shown by comparing case 1 (Figure 2.3, set B) with case 13 (Figure 2.3, set C). In case 13, helium was used as the "light" medium instead of air. The higher sound speed in helium increases the speed of the reflected/transmitted shock waves that resulted from the incident shock wave interacting with the initial inclined interface. Accordingly, the arrival times for the reflected shocks change and ultimately result in the suppression of the large secondary structures seen in case 7 (Figure 2.3, A2). In this case, the λ-shock wave was not destroyed and after its second refraction, smaller secondary structures are created. The authors note that the strength of the refracted shock in case 13 was weaker than that of both case 1 and case 7, but its interaction with the relatively flat $Helium - SF_6$ interface makes the secondary structures more visible [18].

The effects of interface inclination can be seen by comparing case 1 (Figure 2.3, set B) with case 3 (Figure 2.3, set D). The less oblique angle in case 3 provides particularly uniform properties in the post-shock SF_6, due to the weak reflected compressible effects (Figure 2.3, D5). This case is characterized by slower interface growth and a smaller, less-mixed, wall-bounded mixing region [18]. The weakness of this flow results in a simpler interface that contains less secondary spikes and limited mixing. Even so, they noted that a weak Winkler-type vortex can be seen

within the slug (Figure 2.3, D5). McFarland et al. [18] showed that the post-shock flow field is sensitive to the details of the initial shock refraction problem. The Richtmyer impulsive model scaling adapted in their work poorly predicts the early time growth rate for the mixing width and they proposed and an alternative scaling method. This was the inclined interface scaling (IIS) method, which collapses data for different incident shock wave Mach numbers, and interface inclination angles, quite well at early times, due to the use of more detailed information on the shock refraction problem. They hoped to shed light on the secondary effects at late times with their future experiments coupled with further simulation work. The models just discussed regard the interaction of an oblique shock with certain perturbed interfaces.

Now, a discussion of the interaction of a shock with a cylindrical gas column will be presented. Combining the two, i.e. the interaction of an oblique shock with a cylindrical column, is the main focus of this thesis. Once the mechanisms involved with a shock accelerated gas column are presented, a discussion of the most recent numerical studies of the oblique/gas column interaction will lead into our work.

2.2 Early Experiments - Gas Column Interaction

As mentioned before, most RMI experiments have been confined to the interaction of a planar shock interacting with initially perturbed interfaces. RMI, however, may occur at any initial interface arrangement. Within this section, a specific arrangement of the initial conditions, i.e. a cylindrical gas column, will be discussed.

Vorobieff and Kumar [16] addressed the case of cylindrical gas column initial conditions, in 2004. They considered a small perturbation of a diffuse planar interface separating a light and heavy gas, causing the heavy gas to "bulge-out" [16]. A schematic of this is shown in Figure 2.4. They summarized that depending on the direction of the shock, i.e. light-to-heavy or heavy-to-light, the amplitude of the

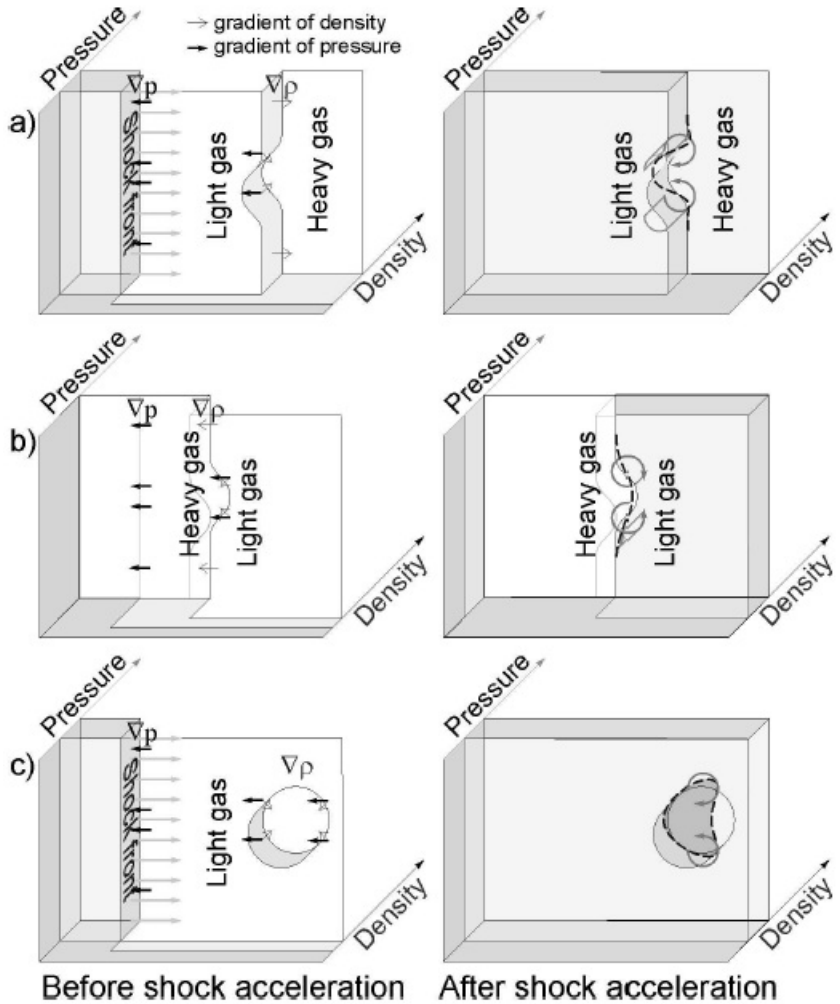

Figure 2.4: Schematics of the initial evolution of RMI-unstable interfaces: a) planar interface with a small "bulge" of heavy gas, shock propagates from the light gas into the heavy gas; b) planar interface with a small "bulge" of heavy gas, shock propagates from the heavy gas into the light gas; c) cylindrical column of heavy gas [16].

perturbation will grow immediately, or after phase inversion, respectively.

The initial conditions here were nominally two-dimensional. However, comparison of late-time flow statistics between experiment and numerical simulations elucidated the limitations inherently present in a two-dimensional simulation of spatially three-

dimensional flow, even if the large scale flow structure is nominally two dimensional [24]. The vorticity deposition in this case produces a pair of counter-rotating vortices whose roll-up is caused by the initial misalignment between the gradient of pressure and the gradient of density [16]. In the case of a gas cylinder (Figure 2.4c), two-fold development occurs: on the upstream side, the perturbation grows immediately, and on the downstream side, the perturbation grows after inversion. The case of the gas column was also studied by Palekar et al. [24] a few years later. In particular, they considered the light-to-heavy case.

The development of RMI can be divided into four distinct stages. The first of which is an initial nearly-linear period of time where the incident shock wave collides with the perturbed material interface and bifurcates into a transmitted shock and reflected wave. From the misalignment of the pressure and density gradient, as mentioned earlier, a baroclinic vorticity will be deposited at the interface, leading to the growth of the perturbation amplitude. The flow-field in this stage is deterministic. This stage is followed by a slightly longer interval of deterministic, non-linear instability amplitude growth during which the morphologies characteristic of RMI develop, with the counter-rotating vortex pairs distorting the interface into patterns of "bubbles and spikes" [16]. To recall, a "bubble" is a portion of the light fluid penetrating into the heavy fluid and a "spike" is a portion of the heavy fluid penetrating into the light [8, 25]. The flow is now non-linear due to the fact that the amplitude of the perturbation has grown to the order of the wavelength. At later times in this stage, material begins to roll-up into the vortex cores. Also, secondary instabilities begin to appear. In the third stage of development, the secondary instabilities begin to dominate and lead the flow to the onset of turbulence via chaotic mixing in the fourth and final stage [16]. Figure 2.5 illustrates these stages.

Many experiments regarding the behavior of the RMI of a diffuse cylindrical gas column interface have been done and several methods of visualization have been used,

Figure 2.5: Stages of the evolution of an RMI-driven flow evolving from initially diffuse, nearly 2D cylindrical initial conditions. Flow direction is from left to right. The dark field corresponds to lighter gas. 1 - initial nearly-linear perturbation growth, 2 - deterministic vortex-dominated growth, 3 - onset of secondary instabilities and emergence of disordered elements in the flow, 4 - transition to turbulence [16].

including PLIF, Rayleigh Scattering, and Mie scattering [2, 15, 16, 28, 27]. Until recently, a full 3D modeling of the shock tube flow developing after acceleration of a gas cylinder was not performed. An investigation by Anderson [2] revealed many interesting features. Notably, the shock-accelerated gas column did not retain its shape in the vertical streamwise plane, from top-to-bottom [26], due to the diffusion of the heavier SF_6 into its surrounding medium of air, and because of the shock interaction with the injection holes. In order for numerical simulations to match the highly repeatable experimental results, an accurate definition of the initial conditions was critical. Anderson used the ANSYS CFD code, FLUENT [31], which employs mass diffusion principles and takes into account viscous effects to model the initial conditions and then imported them into another code, SHAMRC (refer to [2] for details). The results showed that as the column fell, the core of high density narrowed and the diameter of the entire column expanded [2], consistent with previous experimental results [26, 29]. After some initial simulations, Anderson recognized that the simulated instability was much larger than that of the experimental. This was due to the fact the experimental initial conditions actually qualify as a particle laden flow [2, 15, 17] and he then took that into consideration. With this modification, much greater correlation between the experimental and numerical results were

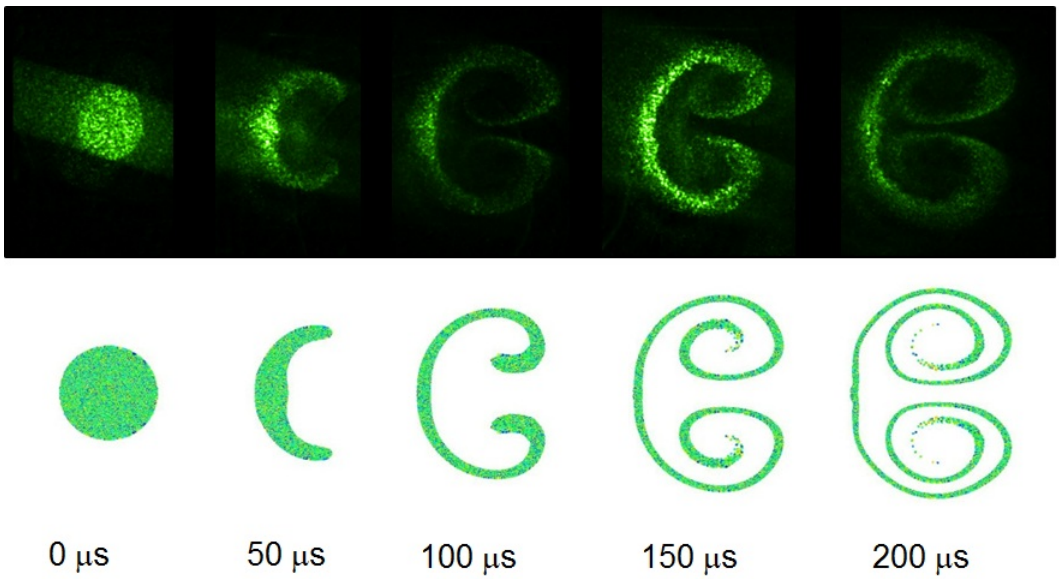

Figure 2.6: Comparison between particle images from SHAMRC (bottom) and experimental images (top) for early times at M=1.22 [2].

observed. The simulations almost mimic the results of the experiment. Figure 2.6 shows this agreement. The top row is a composition of experimental images, using a SF_6 column seeded with simulated tracer (glycol drops), with the plane of visualization oriented horizontally in the middle of the shock tube, and the bottom row is the result of the SHAMRC simulation taking into account solid particles. Anderson then performed a series of simulations to test how certain parameters, like the Atwood number (Equation 1.2), the Mach number, or the particle size, affected the growth of the instability and both of which were shown to significantly impact the behavior of the flow [2].

2.3 Multi-phase Fluid Instabilities

Classically, the initial conditions used to study the development of the RMI of gas-column cylinders have been a mixture of SF_6 and glycol droplets [15, 16, 24, 27], yielding an effective Atwood number of A$\sim$0.67 (Equation 1.2). However, this Atwood number is considered rather "large" and experiments have shown that reducing the Atwood number significantly affects the flow morphology [1]. Vorobieff et al. [16] addressed this case by creating a column of air seeded with glycol droplets [1], yielding an effective Atwood number of A$\sim$0.03. This mixture, referred to as the glycol droplet-seeded air column mixture, however, has a different mechanism acting to produce the vorticity deposition, and is referred to as the Particle Lag Instability (PLI) [1]. The lack of a significant macroscopic density gradient, $\vec{\nabla}\rho$, led the authors of [1] to conclude that the vorticity deposition is not due to the misalignment of the pressure and density gradients, but more so a result of the lagging particles in shocked two-phase media. These lagging particles slow down the embedding gas, producing shear and vortex roll-up. [1]. A schematic of the mechanism is shown in Figure 2.7. After Vorobieff et al. [16] successfully gathered and composed a series of experimental images of this type of instability, Anderson developed a simulation of this specific case [1, 2]. Anderson took two approaches here: 1) model the flow as shock-driven mixing of two gases of different densities with an initially diffuse interface, and 2) model the flow using massive interactive particles. The former of which employs that the air-droplet mixture is modeled as an ideal gas, slightly heavier than the air surrounding it and used the same approach as modeling classical RMI (Figure 2.6). The latter approach was set up so that each computational particle represented a cloud of droplets with the same diameter. In modeling the momentum exchange between heavy particles and the surrounding gas, the representative number of micron-sized computational particles was 100,000 [2]. A compilation of images resulting from several "shots" of the experiment and this simulation are shown in Figure 2.8. Both

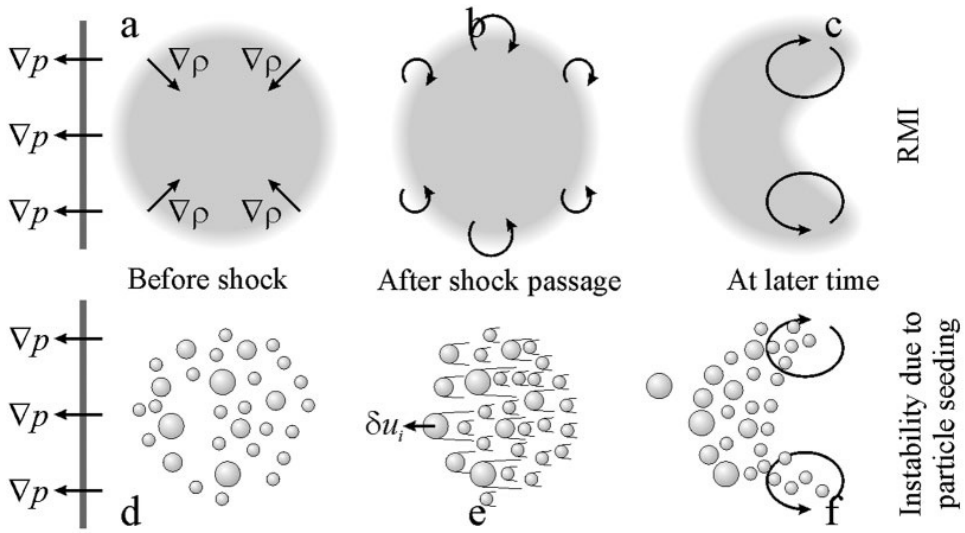

Figure 2.7: Schematic demonstrating the mechanism in which the vorticity develops for the two mixtures. The top row shows the mechanism for which the classical RMI vortices develop. The bottom row shows the mechanism for which the instability of the RMI analog, referred to as Particle Lag Instability (PLI), develops [1].

numerical approaches yielded rather good agreement with the experimental images. Notice the difference in morphology when compared to the classical RM instability experiment of Figure 2.6. Not only is the development much slower, but the overall growth of the instability is much smaller. This "growth" will be discussed in detail in Section 5. Nonetheless, the results appear very similar to that of the classical RM instability case.

2.4 Three-dimensionality Effects

The nominally 2D geometry of initial experimental conditions led to an assumption of two-dimensionality for the initial experimental work. Anderson sought to address the validity of this assumption by performing a series of simulations (and experiments) in the vertical plane oriented in the direction of the shock tube. It was hoped

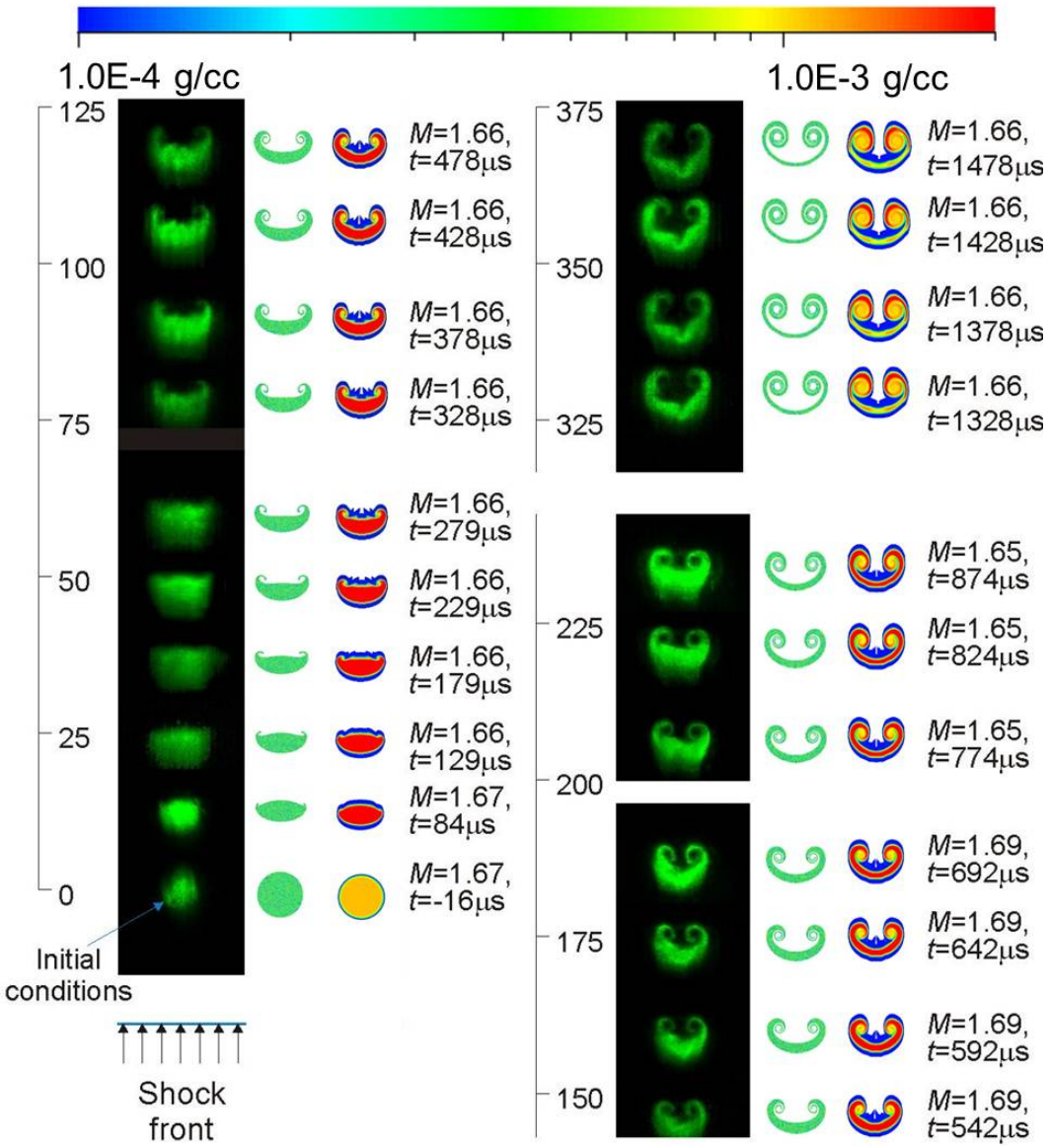

Figure 2.8: Instability Evolution. Green images - experiment (planar laser visualization), color images - numerics. Scale left of the images indicates downstream distance in mm, labels to the right are timings and Mach numbers of experimental images [2].

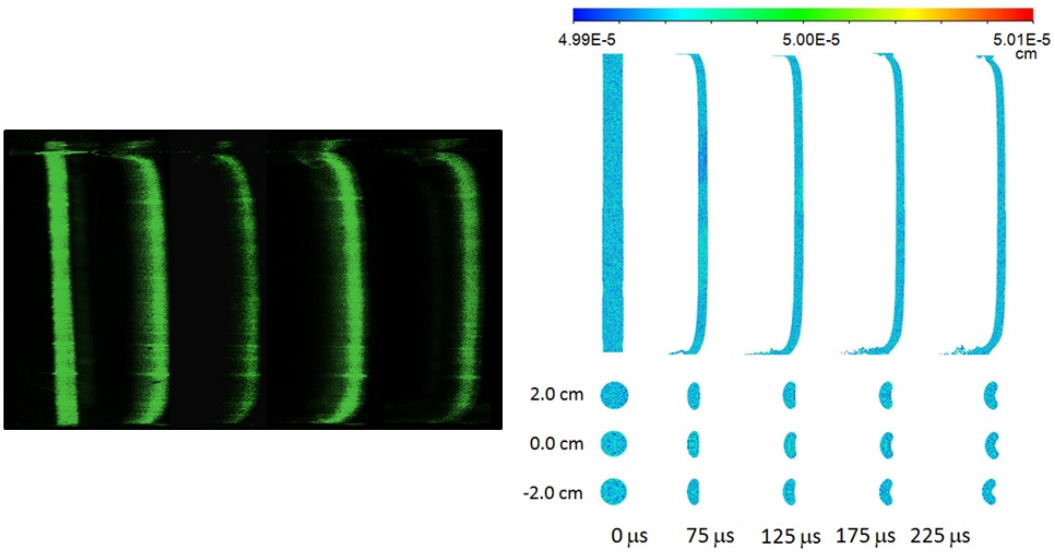

Figure 2.9: Comparison of the experimental (left) and numerical (right) results of the PL instability, viewed in the vertical or "side" orientation [2].

that this "side-view" would confirm the validity of the assumption that the initial conditions were indeed two-dimensional. He performed this test on both the classical glycol droplet-seeded SF_6 column mixture and the glycol droplet-seeded air column mixture. These results are shown in Figures 2.9 and 2.10, respectively. Along with simulating this vertical plane, he also looked at different horizontal planes, whereas previous experiments considered only the horizontal plane oriented in the center of the test section, i.e. equi-distant from both the top and bottom walls. His research supports the assumption that the initial conditions can be considered nominally two-dimensional but only far from the walls. At the walls themselves the flow is seen to lag behind the piston flow, with the cylinder material moving in a pattern that cannot be explained by boundary layer effects alone. Also, the density gradient becomes weaker as the column of falls [2], changing the morphology of the instability changes.

Anderson then considered the novel case of an oblique shock wave interacting with a gas column-cylinder. Experimentally, the shock tube was tilted to a 15° angle with the horizontal but numerically, the gas-column was tilted to 15° with respect

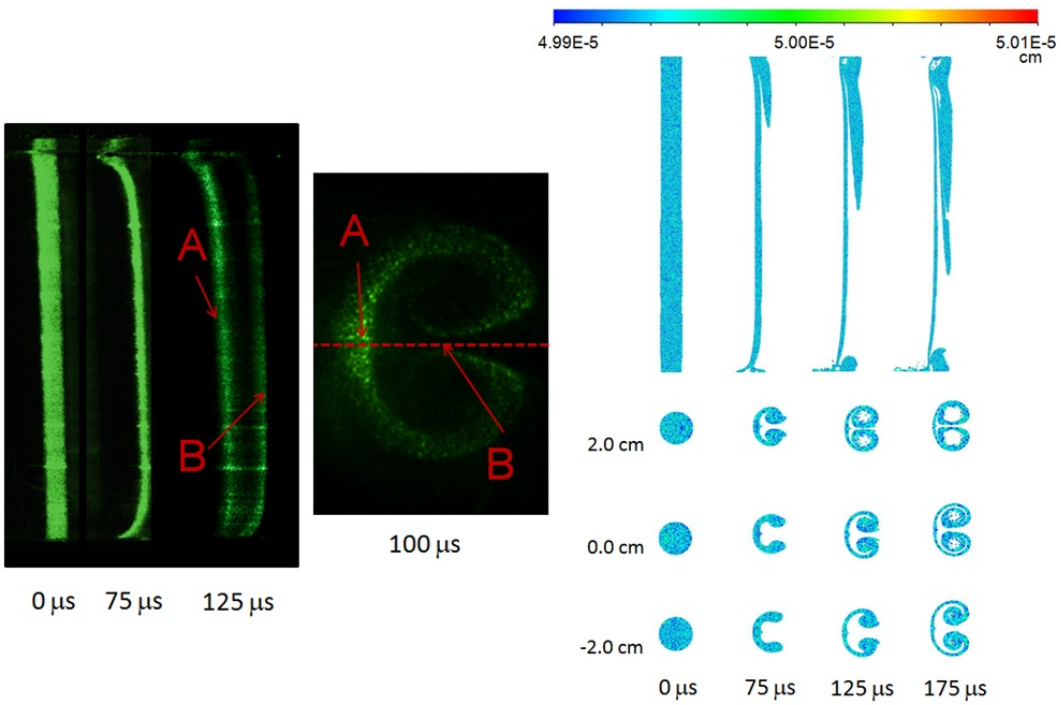

Figure 2.10: Comparison of the experimental (left) and numerical (right) results of the RM instability, viewed in the vertical or "side" orientation [2].

to the boundaries of the computational domain [2]. Anderson studied both the classical glycol droplet-seeded SF_6 column mixture and the glycol droplet-seeded air column mixture and the results are shown in Figures 2.11 and 2.12. Once again, good agreement was seen between the experimental and numerical results. The major difference here, however, is seen at the upper and lower boundaries. It is observed that much more of the column gets entrained into the flow near the wall areas. This Thesis covers the experimental study of shock accelerated single and multi-phase initial conditions at an oblique angle of 15°. Chapter 3 presents the experimental methods used, while Chapter 4 discusses the post processing techniques used. Chapter 5 covers the experimental results. Chapter 6 draws conclusions on the experimental results and Chapter 7 will summarize and allude to possible future research.

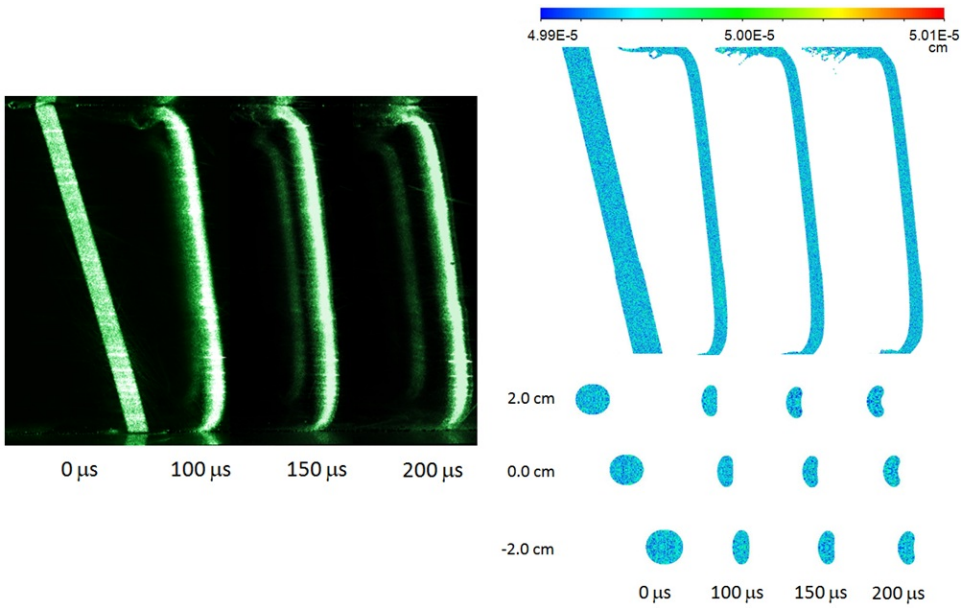

Figure 2.11: Comparison of the experimental (left) and numerical (right) results of oblique PLI, viewed in the vertical or "side" orientation [2].

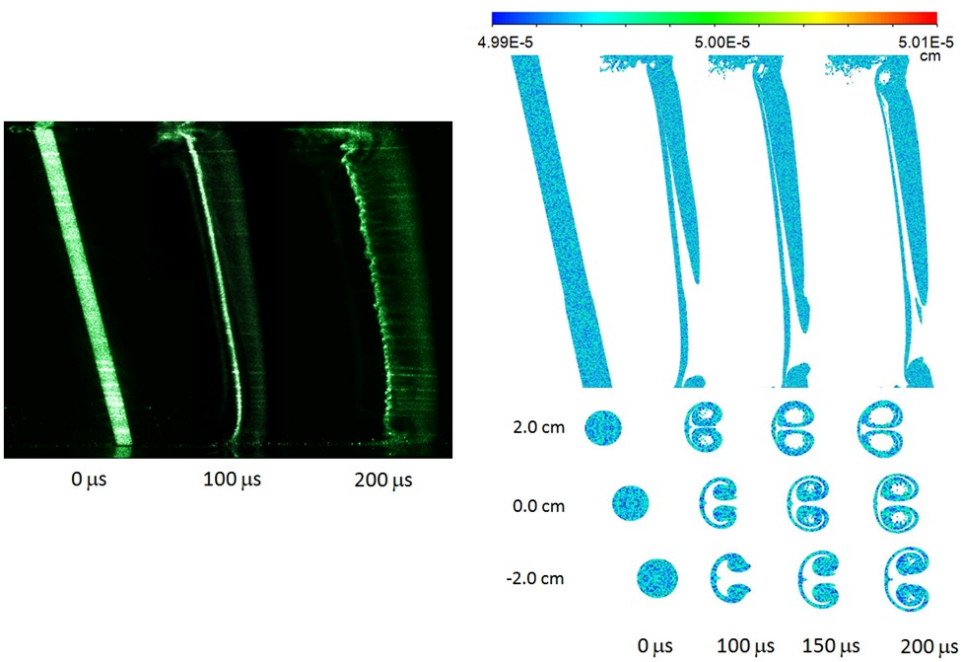

Figure 2.12: Comparison of the experimental (left) and numerical (right) results of oblique RMI, viewed in the vertical or "side" orientation [2].

Chapter 3

Experimental Set-up

The experiments discussed throughout this thesis were performed at the University of New Mexicos Mechanical Engineering Shock-Tube laboratory. This chapter will describe the facility and the equipment used during the experimentation process.

3.1 Shock Tube

The shock tube is comprised of four sections: the driver, the driven, the test, and the run-off sections, see Fig 3.1. The driver, driven and run-off sections are all made of 6061-T6 Aluminum and the test section is made of Lexan. Each section has 6061-T6 Aluminum flanges attached to their ends drilled with octagonal bolt patterns. The shock tube is tilt-able up to 30° from the horizontal, allowing for the study of oblique shock wave interactions. The driver section uses a circular, 3.75 inch (9.53 cm) outer diameter tubing with a 0.5 inch (1.27 cm) wall thickness. The reason for the circular driven section is to avoid high stress concentrations during the highly repetitive experimental procedures [27]. Within the driver section a 0.25 inch (0.64 cm) shaft is positioned concentrically and has a puncturing device mounted on its downstream

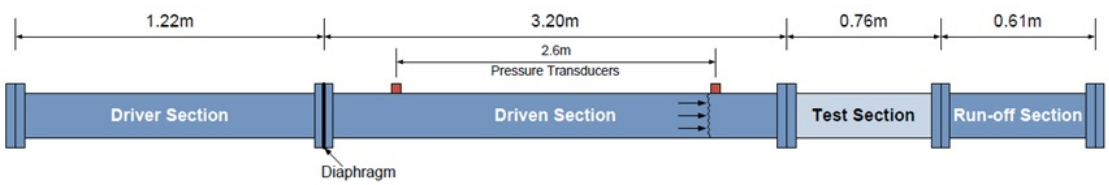

Figure 3.1: Schematic of Shock Tube. [27]

end. The puncturing device is an assembly of four razor blades mounted 90° apart from each other, creating a four-pointed star shape. This arrangement aids in the puncturing of the diaphragms in experiment. Figure 3.2 shows the puncturing device mounted on the shaft within the driver section. The other (upstream) end of the shaft is connected to an electronic solenoid which is used to actuate the puncturing device. For the entirety of this thesis, each time a diaphragm is punctured, sending a shockwave down the shock tube, and initializing the diagnostics (discussed in the next section), will be referred to as a "shot". The driver section is then connected to the driven section. This is done by using two custom modified clamps, one on each side [28]. This design allows for fast changing of the diaphragms, greatly increasing the productivity of the experimental process. The driver section is constructed of 4 inch (10.17 cm) square 6061-T6 Aluminum with a 0.5 inch (1.27 cm) wall thickness. It has two pressure transducers mounted on its top side, one upstream and one downstream, see Figure 3.1. These allow for a measurement of the shock speed and allow the experimenters to observe the quality of the shock wave itself. They also act as the trigger for our visualization techniques, discussed in the next section. The test section is attached to the downstream side of the driven section. The test section is built from 4 inch (10.17 cm) square polycarbonate with 0.5 inch (1.27 cm) wall thickness. The usage of Lexan allows for undistorted imaging of the phenomena that occur during experiment. The test section has holes drilled through it so the initial conditions are able to flow through the section. The injection system attaches at these holes and will be discussed in the next section. With a tiltable shock tube, a

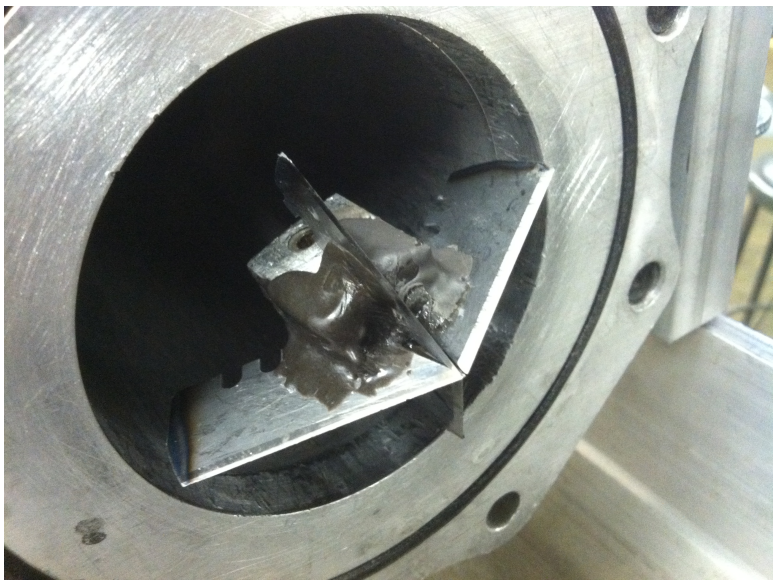

Figure 3.2: The four-pointed star puncturing head, mounted in the driver section.

test section is specifically manufactured for a particular tilt angle, i.e. for a 15° tilt, a 15° hole is cut, for a 30° tilt, a 30° is cut, etc. The run-off section is then attached to the downstream side of the test section. This sections purpose is to ensure that the shock holds its shape long after it passes the area of interest in the test section. The shock tube itself sits on a rail system comprised of a combination of C and I-beams that are attached to a solid concrete wall at the "lower" or downstream end of the shock tube. This keeps the shock tube stationary during experiments [28] and allows background subtraction during image processing.

3.2 Injection System

The initial conditions of the experiments discussed in this thesis are cylindrical gas columns. For visualization purposes, tracer particles are required to be mixed with the flow. In order to mix tracer particles with a particular gas, air or SF_6, a 30 gallon

(12"Wx20"Lx16"H) fish tank is used. A recreational fog (smoke) machine, is set atop this section with its exit nozzle directed down into the fish tank. Activation of this machine via push-button remote, floods the chamber with fog, which is comprised of sub-micron sized water-glycol droplets that can be illuminated using a number of visualization techniques. Upon exit of the fog machine, the water-glycol droplets are at a high temperature and to avoid the buoyancy affects associated with such, a bucket of ice is placed in the chamber. This acts as a cooling and mixing agent, encouraging temperature equilibrium between the injected mix and the ambient air. Temperature in the chamber is monitored with a digital thermometer. The gas-droplet mixture is fed down through the test section via a cylindrical apparatus, composed of a 0.23 inch (0.6 cm) diameter steel cylinder, through which the gas mixture travels, and a 0.5 inch (1.27 cm) sheath attached on its exterior. This sheath acts as a vent for air at atmospheric pressure to co-flow with the gas mixture and provides a stabilizing effect [27]. A schematic of how this works is presented in Figure 3.3 [27]. The glycol droplet seeding density necessary to provide an effective Atwood number of 0.03 is less than 5% by volume. Thus the subsequent particle-air interaction is to be expected to be a "two-way" coupling in the classification of Elgobashi.

3.3 Diagnostics

An Apogee high performance cooled CCD camera system, the Alta U42, is used to capture the interaction of the shock wave with the gas cylinders. This model has a back-illuminated full frame 4-megapixel CCD with exceptionally high quantum efficiency. The standard mid-band coating has the highest peak in the visible wavelength range, specifically at 532 nm. The camera can be oriented to view both top and side views of the test section, allowing for perpendicular plane images of

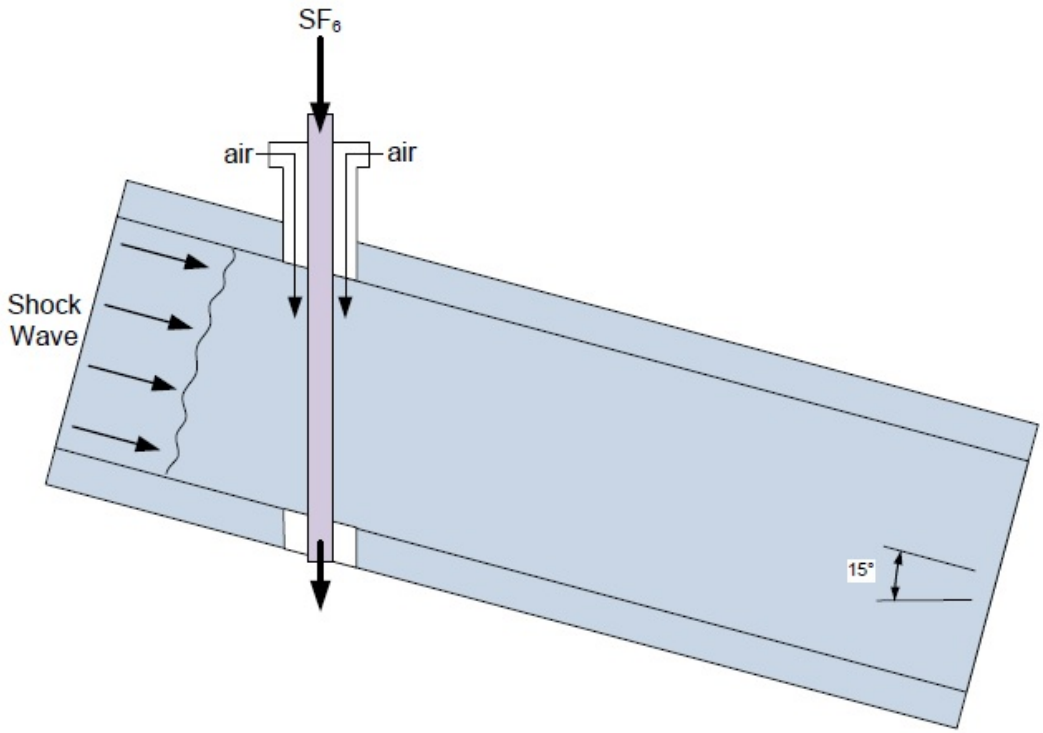

Figure 3.3: The injection system with co-flow implemented for the oblique shock tube arrangement. The fish tank chamber and fog machine apparatus sit above where SF_6 flows in (top of image) [27].

the shockwave/gas-cylinder interaction to be observed. See Figures 3.5 and 3.6. Although the camera has superb resolution, it can only capture one exposure over the time interval of shot.

To achieve visualizations of the shock-wave/gas-cylinder interactions, a set of Nd:YAG lasers are used [30]. For particle visualization, 532 nm frequency-doubled pulses are used, with each pulse producing up to 100 mJ optical energy, and with a pulse duration not exceeding 5 ns. The laser pulses are triggered by the pressure transducers attached to the driven section discussed previously. The shock wave sets off these pressure transducers. The shock arrival at the second transducer is used to trigger the camera and lasers. The pressure traces are recorded using the software

Figure 3.4: Apogee Alta U42

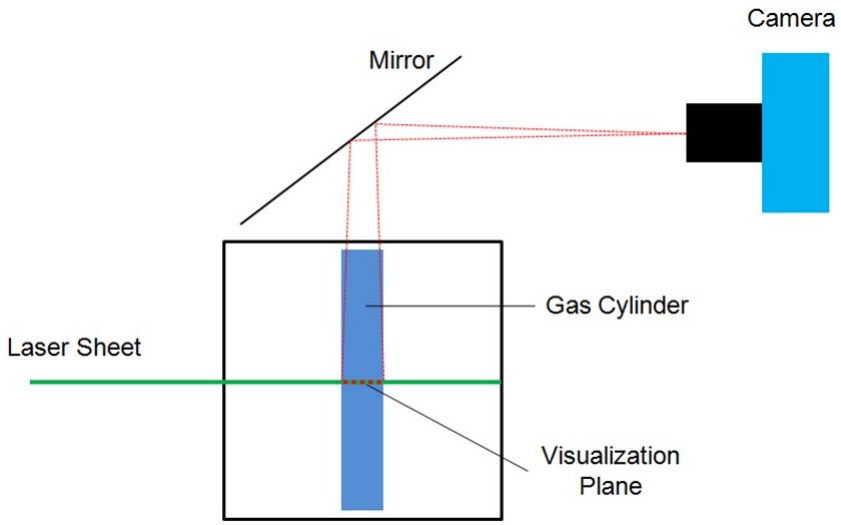

Figure 3.5: Camera orientation for acquiring images from the Top-view, i.e. horizontal planes. [2]

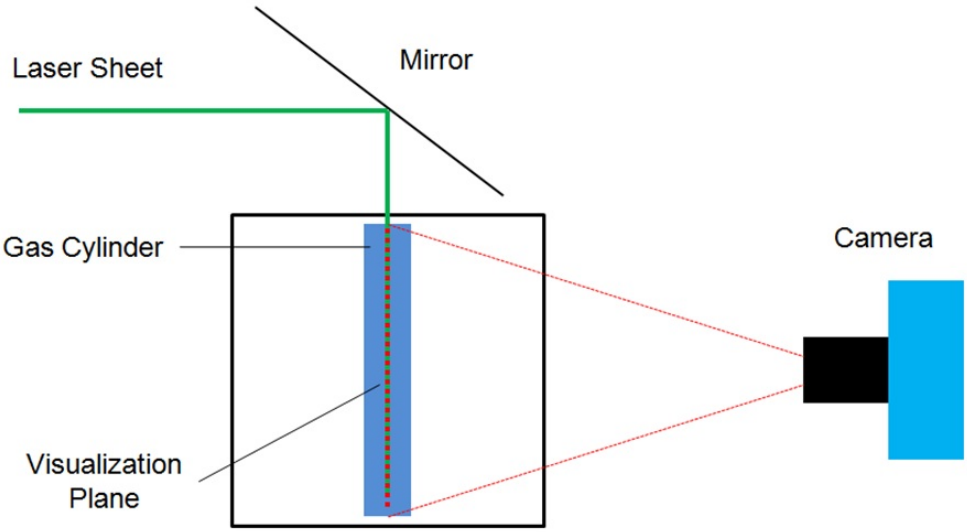

Figure 3.6: Camera orientation for acquiring images from the Side-view, i.e. Vertical planes. [2]

Ni-Scope (National Instruments) [32]. The delay generator acts as the timer for the laser pulses and can be easily adjusted to capture various times of interest. The laser pulses themselves act as the "flash" for each exposure. Imposing a delay between each laser pulse allows for the ALTA U42 single exposure to essentially capture two or more images per shot, greatly increasing productivity of the experimental process. The laser sheets are formed by passing the laser beams through a combination of a cylindrical and a spherical lens, both mounted on an optical rail attached directly to the tripod-mounted laser head assembly. With a mirror and an appropriate orientation of the cylindrical lens, the laser sheet can illuminate a vertical plane or a plane tilted at the same angle with horizontal as the shock tube. In our experiments, both orientations were used.

3.4 Diaphragms

During the experiments a diaphragm is punctured, releasing the pressure from the driver section and sending a shock wave down the driven section to the test section where the diagnostic cameras, etc. are employed. Accordingly, the diaphragm needs to be able to hold high pressures but at the same time rupture in a quick and well-defined manner. In our experimental facility, several types of diaphragms have been used for varying driver section pressures [27, 28]. For low pressures, i.e. relatively weak shock waves such as $M = 1.2$, photograph paper performs well, but for higher pressures Mylar diaphragms were used. In particular, 3M's CG5000 Dual-Purpose transparencies, proved to fit our needs quite well. As higher pressures are needed (for higher Mach number shock waves), just add additional transparencies. In order to try and reduce waste (not necessary, but ethical) another type of transparency, 3M's CG6000 Universal Transparency Film, was also used.

3.4.1 Observations on the Transparencies

Mach number shots of $M = 1.67$ are the main focus of this thesis. This corresponding chamber pressure was used as the base parameter for testing the CG6000 transparencies. It was found that the CG6000 transparencies would hold the needed pressure using only 1 transparency (as opposed to the 2 needed to do the same with the CG5000 transparencies). To measure how well the diaphragms ruptured, pressure traces from the pressure transducers on the driven section (Section 3.1), were obtained. The pressure traces of the CG5000 and the CG6000 transparencies are shown in Figure 3.7. Notice there is little differnce between the two traces, only the graph on the left (CG5000) is slightly more noisy than that of the right (CG6000). It is seen that the "quality" of the shock wave is similar for both transparencies but only half as many are needed to achieve the desired performance.

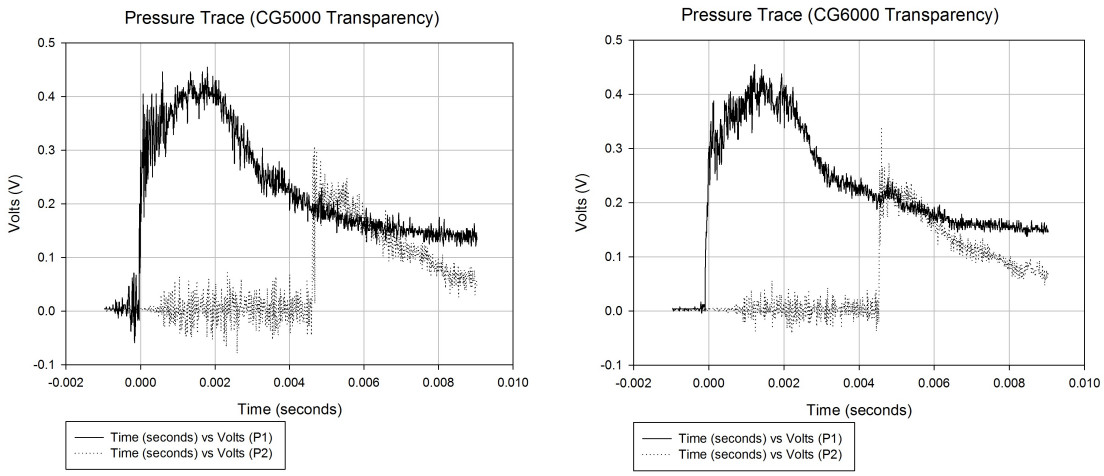

Figure 3.7: A comparison of the pressure traces that each diaphragm produced.

Using fewer transparencies per shot came with a trade-off, however. The CG6000 transparencies have a coating on one side that is brittle and "flakes" off rather easily. When these diaphragms were ruptured, this coating shattered into small particles that got entrained into the flow and nearly travel at shock speed. The left image of Figure 3.8 shows these particles arriving at the initial conditions just after the shock has passed; it can be seen that the particles are evenly distributed throughout the shock tube.

At later times ($t \geq 600\mu s$), the particles can be seen to have passed the instability but seem to be small enough not to affect the morphology of the instability. The right image of Figure 3.8 shows the presence of these particles at late times. Although the presence of the particles makes the obtained images more noisy, they do not affect the flow characteristics and can be neglected when considering the instabilities themselves. The following chapter will discuss the techniques used during post-processing of the experimental data, leading to the results of the experiments.

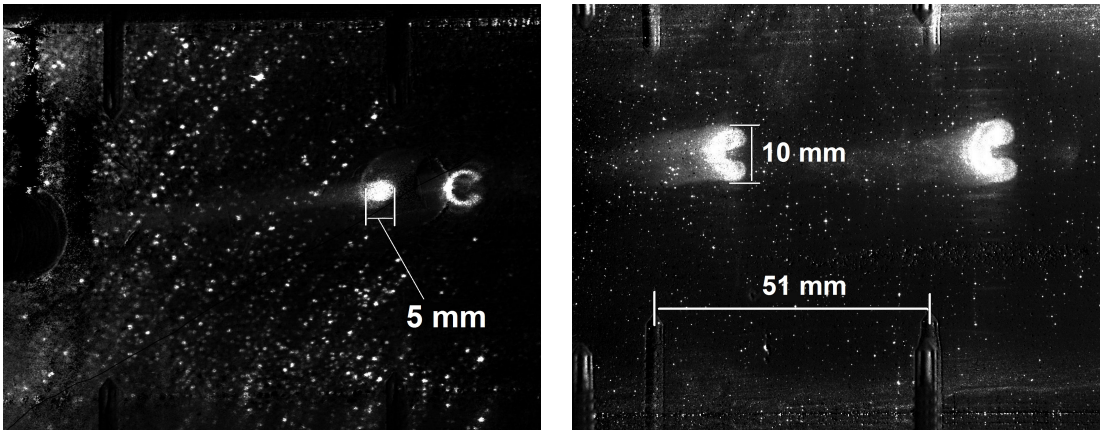

Figure 3.8: The presence of the small "flake-like" particles in the flow that break off the CG6000 transparencies. (Left) Early times, approximately 50 μs between exposures. (Right) Late times, approximately 150 μs between exposures.

Chapter 4

Post Processing Techniques

For each shot, several diagnostic devices were used. In order to reduce the raw data acquired from the devices, various post-processing techniques need to be employed. The following subsections will discuss the major techniques used.

4.1 Spanwise and Streamwise Measurements

For the data presented, two measurements will be referred to repeatedly: spanwise and streamwise sizes. When measuring the growth rate of the instabilities, we measured with respect to the side-to-side direction (spanwise) and the upstream-to-downstream direction (streamwise). Figure 4.1 demonstrates these measurements. The reason these measurements are used is because the majority of experiments regarding shock wave interaction with gas column cylinders use these same directions for quantification purposes and therefore allow our experiments to be compared with earlier works. Typically, the spanwise size grew immediately after the shock passed and continued to grow as time progressed. The streamwise size, conversely, underwent a short stage of compression and phase inversion, which made the measurements

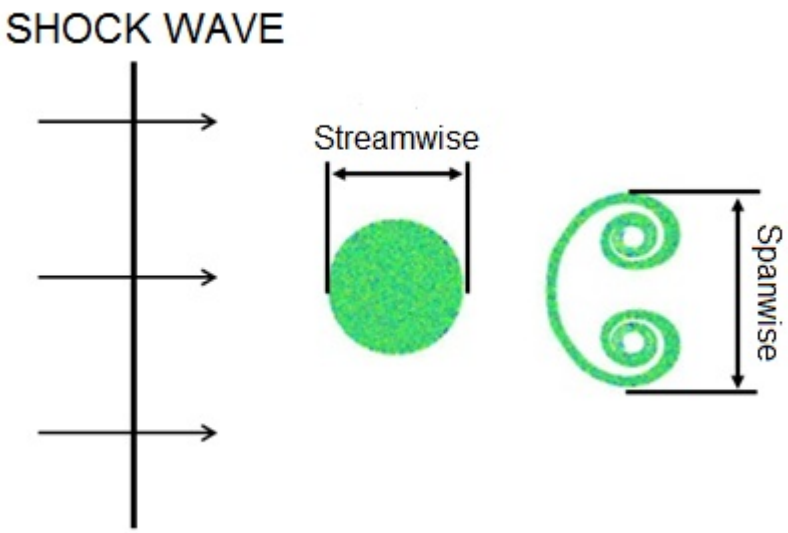

Figure 4.1: Schematic of the orientation of the Spanwise and Streamwise measurements [2].

get slightly smaller immediately after the shock passed and then they grew from there as time progressed.

4.2 Time Correction

One major difference between oblique shock wave interactions with gas cylinders and the planar shock wave interactions [16, 28, 29] with gas cylinders, is the time at which the shock wave arrives. In the planar case, the shock arrives at the same time in all planes of interest. This was not the case, however, for the oblique shock wave interactions. The shock wave impacted the top of the initial conditions before it impacted the bottom of the initial conditions. Accordingly, a time correction was needed for each plane. Figure 4.2 is a schematic of these correction distances. Table 4.1 shows the times associated with the distances in Figure 4.2. The times corresponding to each plane were calculated using a Mach number $M = 1.67$ shock

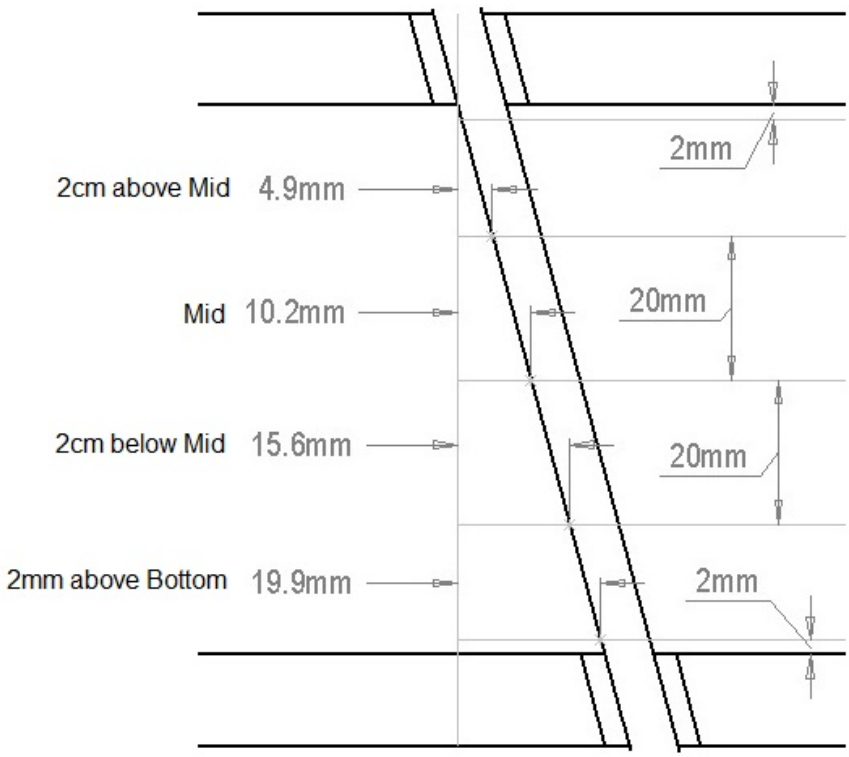

Figure 4.2: The dimensions used for the time corrections.

wave or a 550 $\frac{m}{s}$ shock speed. The worst case time correction is approximately 35μs, which is not extremely significant, but must be taken into account.

Table 4.1: Distance and Time Corrections for the Oblique Interactions at a Mach number of $M = 1.67$.

Plane	Streamwise Distance	Time Correction
2 mm from TOP Wall	0.5 mm	0.97μs
2 cm above Middle Plane	4.9 mm	8.89μs
Middle Plane	10.2 mm	18.5μs
2 cm below Middle Plane	15.6 mm	28.3μs
2 mm from BOTTOM Wall	19.9 mm	36.1μs

4.3 Angle of Camera/Mirror for Early Times

For the early time images (i.e. $0 \leq t \leq 220\mu s$), the camera must be angled to view the gas column initial conditions. The camera was angled because the injection system prevents the camera from viewing a straight reflection from the mirror of the initial conditions themselves. This angle made the images slightly offset from the normal direction of flow. For the images taken at a later time and farther downstream distance, on the other hand, the camera is oriented so its viewframe is parallel with the walls of the shock tube. Hence, the upstream images needed to be processed a step further than the downstream images in order to account for this offset. This process is referred to as deparallaxing and combines removal of rotation, perspective effects, and optical distortions from the image by taking an image of a target (grid) and mapping it to an undistorted image of the same target. The mapping was performed via bicubic interpolation between corresponding grid squares. Figure 4.3 shows the image both before (left) and after (right) this process. If this step were not taken it would be much more difficult to quantify the spanwise and streamwise size measurements due to the angle of the intstability growth. This way, the same measurement processing can be performed on all of the images in the same manner.

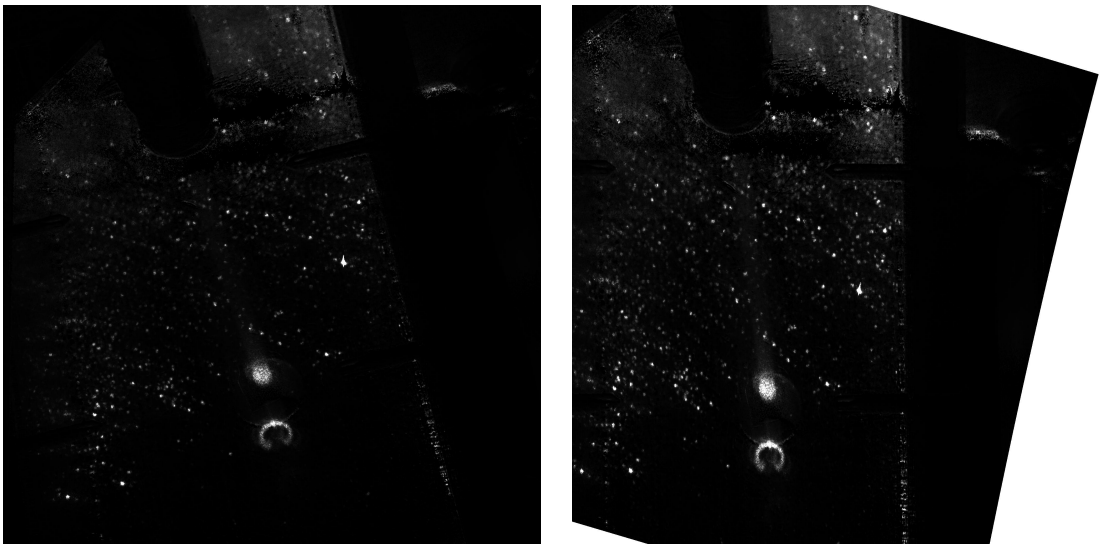

Figure 4.3: Left - a raw image before post-processing. Right - the image on the left after it has been post-processed.

Chapter 5

Results

This chapter will present the results from experiments conducted at $M = 1.67$ and with the shock tube tilted to 15° from the horizontal. An investigation into the morphology of the instability at five different horizontal planes for both the single-phase (RMI) and the multi-phase (PLI) mixtures was performed. The analysis of these shots allowed us to gain new information about the effect of the injection holes. This also broadened our understanding of how the oblique shock wave interacts with the gas cylinder.

Figure 5.1 shows how the shock wave interacts with the gas column. The images are a composition of several shots of the glycol droplet-seeded SF_6 column gas column. The left image is what the initial conditions look like prior to the arrival of the shock. The image second from left was taken just as the shock began to pass the column. Notice how the top third is "bright" white, whereas the bottom half is an evenly distributed gray. This image shows that the shock wave indeed impacts the top of the initial conditions long before the bottom and supports the time correction (Section 4.2) presented above. The two images on the right side of Figure 5.1 are taken at the times shown; approximately 3 inches and 7.5 inches downstream, respectively. The

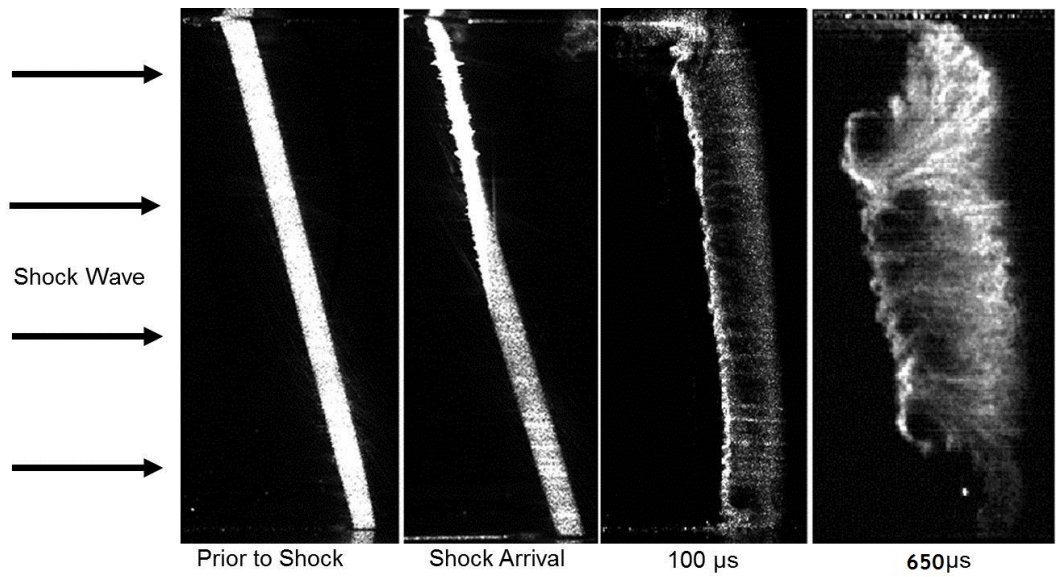

Figure 5.1: The progression of the shock wave through the initial conditions (glycol droplet-seeded SF_6 column). Shock moves from left to right. (Note: in order to see small scale features, the gray-scale of each image has been slightly modified.)

sequence shows how the gas column progresses downstream and how the instabilities develop. To gain an understanding of what is happening at specific planes near and far from the bounding walls, five horizontal planes were studied. The five horizontal planes of interest are the middle plane, 2 cm above and below the middle plane, 2 mm below the top bounding wall, and 2 mm above the bottom bounding wall. The middle-plane refers to the horizontally oriented plane placed along the centerline of the shock tube. The middle plane is 38 mm from either bounding wall and accordingly the plane 2 cm above the middle plane is 18 mm from the top bounding wall and the plane 2 cm below the middle plane is 18 mm from the bottom bounding wall. Of special interest are the planes 2 mm from the top and bottom bounding walls because of the difference in morphology observed in the experiments and simulations of Anderson [2]. The mechanisms in which these planes differ from the rest will be discussed in detail in Section 6.3.

5.1 Classical RMI

Experiments with the glycol droplet-seeded SF_6 column gas column were performed in the tilted orientation of the shock tube at a Mach number of $M = 1.67$. Planar laser visualization techniques were used to visualize the five planes of interest discussed earlier. After post-processing of the images, a collage of several shots were compiled and are shown in Figure 5.2. In this image, the shock is moving from left to right. It can be seen that the morphology of the instability is similar in the three middle planes (i.e. the mid-plane, 2 cm above and 2 cm below the mid-plane) at both the early (left) and late (right) times. In the upper and lower image sequences, however, similarity is seen only in the early times. Large differences are measured/observed further downstream. The top-right image displays a long tail-like structure that fades further upstream, whereas the bottom-right image displays a much smaller instability. A discussion of the mechanisms involved here are discussed further in Section 6.3. Notice the difference in sizes of the instabilities in each plane and note the lack of initial conditions in the top-left image. Unfortunately, with the geometry of the injection system and mirror arrangement, it was impossible to capture images of the initial conditions in the plane 2 mm from the top bounding wall (see Section 4.3). Measurements of the spanwise and streamwise growth rates were taken using an image processing software, *ImageJ*, using the rectangular box tool. Using this tool allowed for simultaneous measurement of both the spanwise and streamwise sizes. These measurements are presented in Figures 5.3 and 5.4, respectively. At these scales, the error of the measurements is on the order of 50-100μm spatially, and 5-10μs temporally. Hence the error bars are left out of these graphs simply because they would be smaller than the data point markers themselves. They will also be left out of the graphs on later pages for the same reasons. From these measurements, it can be seen that the *spanwise* measurement increases immediately after the shock passes and continues to grow as time progresses (Figure 5.3). The

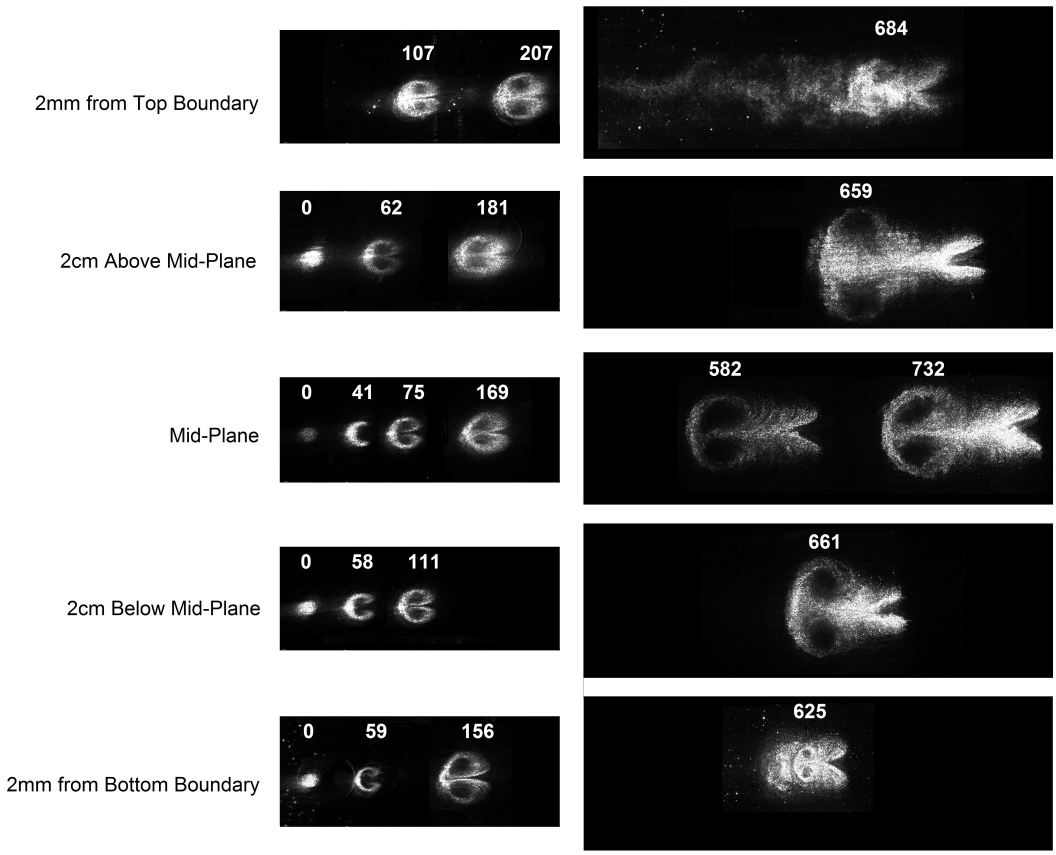

Figure 5.2: Post-processed images of the glycol droplet-seeded SF_6 column at the 5 horizontal planes of interest. The numbers in the images correspond to the time (in microseconds, μs) after the shock hits, with time t=0 when the shock arrives. The shock front moves from left to right. The images on the left are taken as the shock arrives and passes the initial conditions, whereas the images on the right are taken approximately 7 inches downstream of the initial conditions.

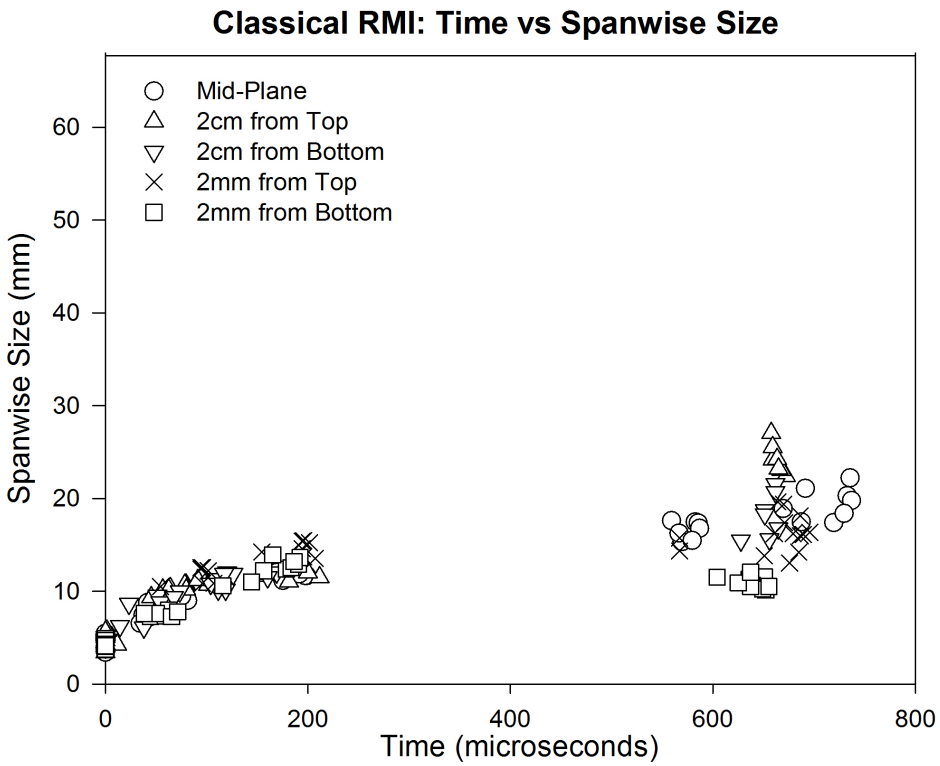

Figure 5.3: Spanwise size of the counter-rotating vortex pair of the glycol droplet-seeded SF_6 column versus time.

streamwise measurement underwent a short stage of compression and then grew as time progressed. These behaviors are typical of the Richtmyer-Meshkov instability and have been observed in a number of studies [1, 2, 16, 25, 26, 29, 15]. Notice how the measurements at the early times (i.e. $t \leq 220\mu s$) are very closely arranged regardless of the plane of interest. At the late times, however, we begin to see large differences in the size of the spanwise measurements and an enormous difference in the size of the streamwise measurements. These measurements are consistent with the observations at the multiple planes (Figure 5.2) and the simulations of Anderson [2]. More details on this phenomenon will be presented in Section 6.3.

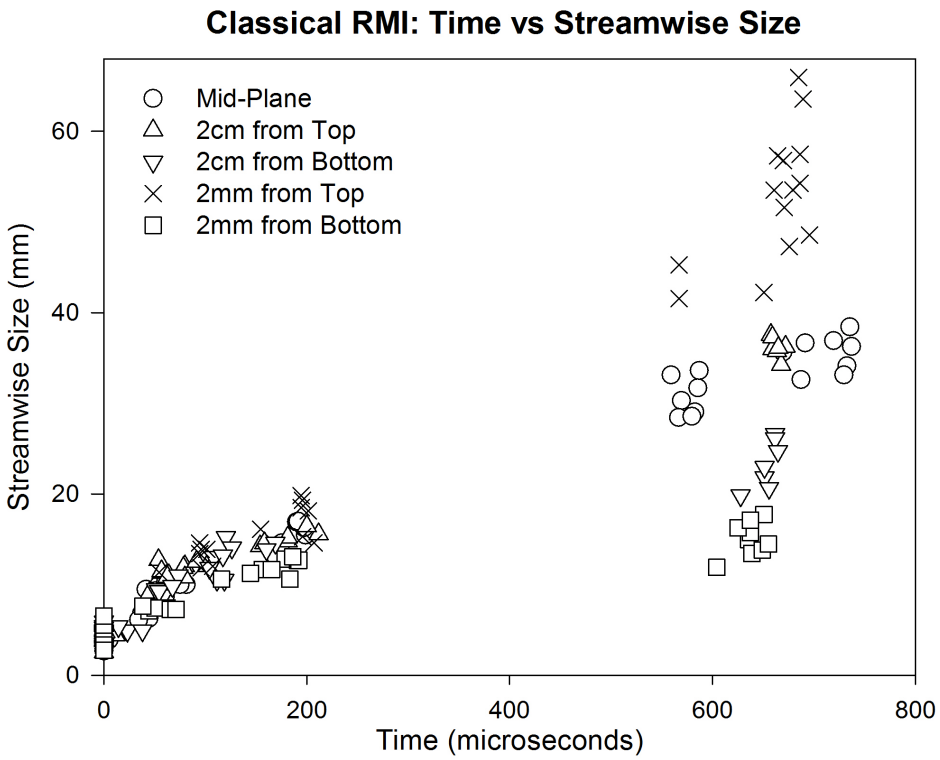

Figure 5.4: Streamwise size of the counter-rotating vortex pair of the glycol droplet-seeded SF_6 column versus time.

5.2 Particle Lag Instability (PLI)

Experiments were also performed on the glycol droplet-seeded air column gas column in the tilted shock tube orientation at Mach number of $M = 1.67$. Planar laser visualization techniques were used to visualize the 5 planes of interest as done with the glycol droplet-seeded SF_6 columns. A collage of images acquired at these planes is shown in Figure 5.5. Again, the shock is moving from left to right. Althought the Particle Lag Instability has a different mechanism causing the deposition of vorticity, similar morphology is observed. Once again, the middle three planes disply very similar development in both the early and late times while the top and bottom images vary immensely. Also, note the lack of initial conditions in the top-left image

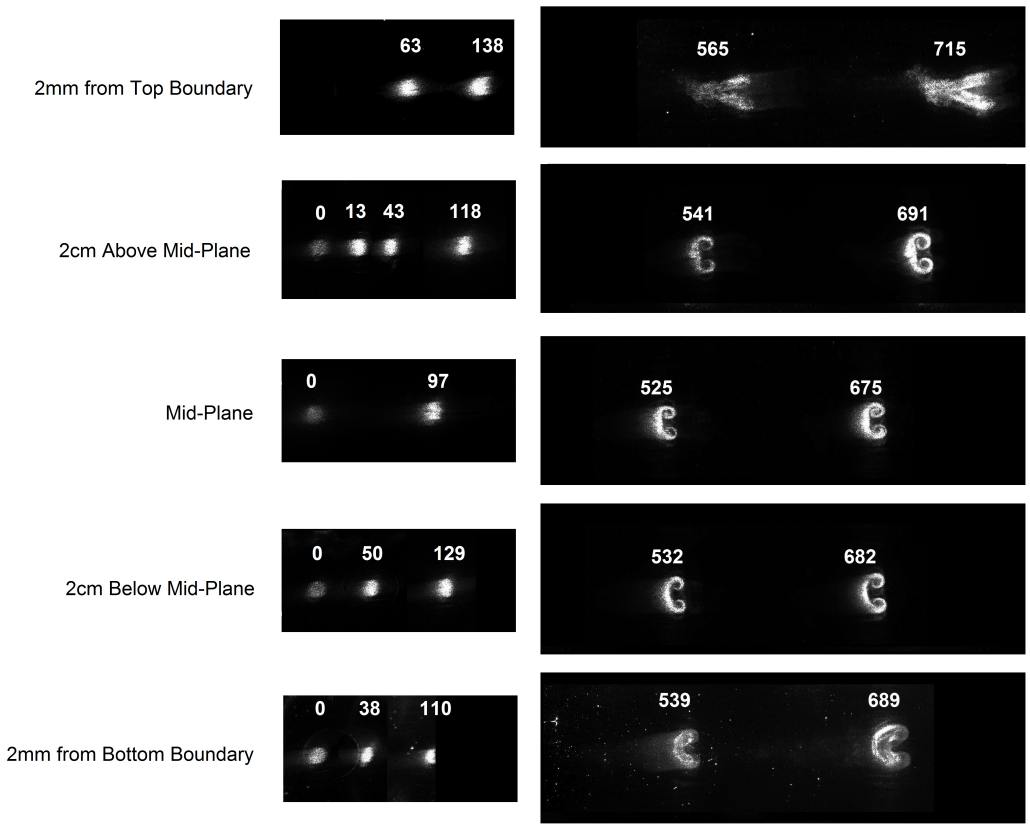

Figure 5.5: Post-processed images of the glycol droplet-seeded air column at the 5 horizontal planes of interest. The numbers in the images correspond to the time (in microseconds, μs) after the shock hits, with time t=0 when the shock arrives. The shock front moves from left to right. The images on the left are taken as the shock arrives and passes the initial conditions, whereas the images on the right are taken 7 inches downstream of the initial conditions.

just as in the top-left of Figure 5.2 (see Section 4.3). Another characteristic of the Particle Lag Instability, is the overal size of the instability itself. Compared to the classical Richtmyer-Meshkov (glycol droplet-seeded SF_6 columns), it is much smaller. A discussion of this characteristic and the mechanisms in which the top and bottom planes develop differently will be presented in Section 6.3. As with the glycol droplet-seeded SF_6 column images, spanwise and streamwise measurements were taken to quantify the growth rate of the developing instability. These measurements are

presented in Figures 5.6 and 5.7, respectively. Here, we observe a similar trend; the spanwise size increases immediately after the shock passage and continues to grow (although at a slightly slower rate) as time progresses. The streamwise size undergoes the same short compression stage, growing thereafter, although it seems this is not as clearly seen in these experiments at the scaling shown.

In both the spanwise and streamwise measurements, the data is closely arranged at early times with differences becoming apparent at late times. The data points indicated by 'x's in Figure 5.7 in the upper right almost seem to be outliers but this is not the case. They are the measurements of the plane 2 mm from the top bounding wall. The instability is so small in all other planes of interest that the tail present in the plane 2 mm from the top bounding wall approximately triples the streamwise size compared to the other planes. This makes the data points indicated by 'x's seem like outliers. The top-right image in Figure 5.5 indicates that there exists a morphology that is different than that of the other planes of interest but does not display the enormously long tail that the glycol droplet-seeded SF_6 columns exhibit.

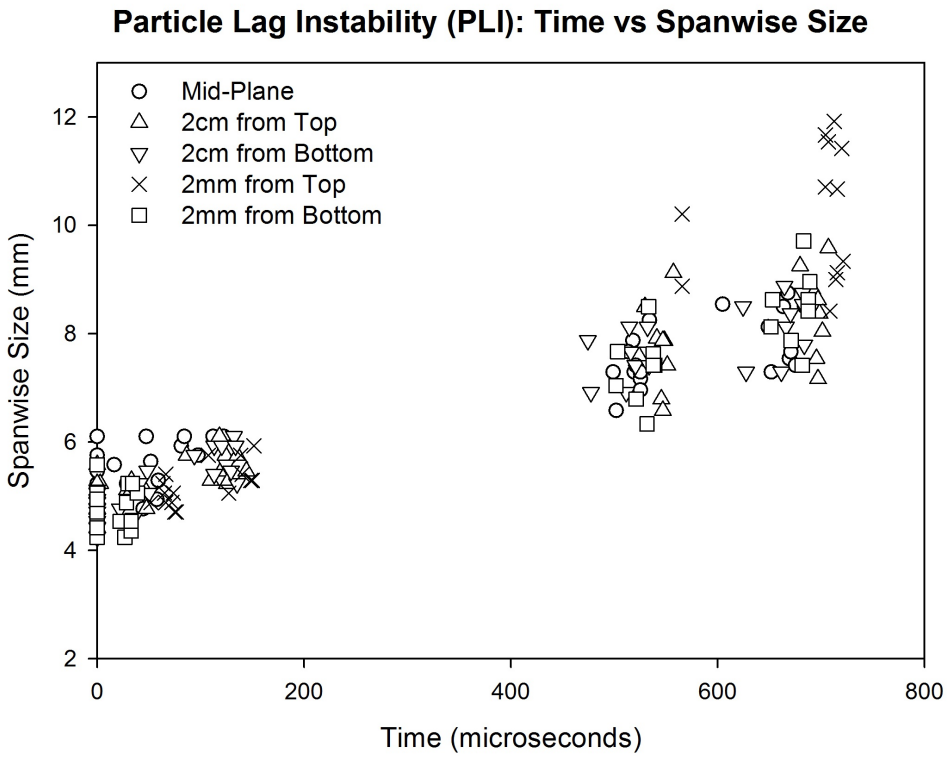

Figure 5.6: Spanwise size of the counter-rotating vortex pair of the glycol droplet-seeded air column versus time.

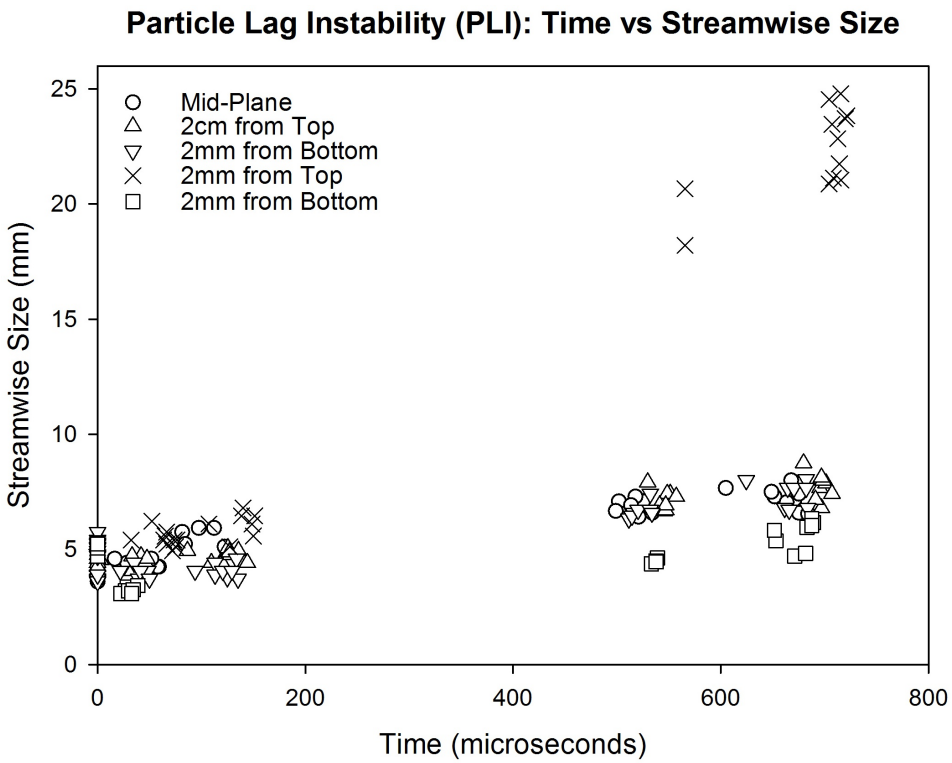

Figure 5.7: Streamwise size of the counter-rotating vortex pair of the glycol droplet-seeded air column versus time.

Chapter 6

Morphology Characterisics

In this section a discussion about the mechanisms influencing the morphology of the different horizontal planes will be presented. As was seen in the previous sections, the morphology of the instability varies from top bounding wall to bottom bounding wall. It was observed that there was a long tail that forms and is entrained close to the top bounding wall, whereas close to the bottom bounding wall this is not observed. Also, the morphology throughout the middle planes, although similar, varies from plane to plane.

6.1 Density Gradient Effects

As the oblique shock wave passes the initial conditions and the instabilities (both mixtures) begin to develop, it was observed that there was significant asymmetrical characteristics occurring. Figures 6.2 and 6.3 demonstrate this asymmetry. The top of the instability is larger (with respect to the streamwise, or left-right direction) than the bottom in the glycol droplet-seeded SF_6 column case. Orlicz [29] postulated that this was due to the high concentration of material immediately after exiting the

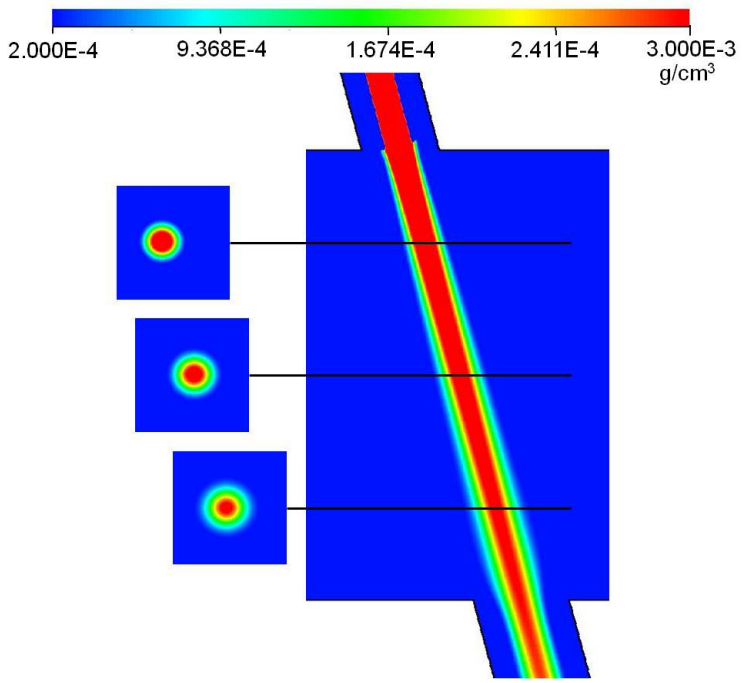

Figure 6.1: SHAMRC density contours of the initial conditions in the vertical plane [2].

injection nozzle [29] that diffuses as the column falls, reducing its concentration and thus lowering the density gradient, $\vec{\nabla}\rho$. This diffusion of the column as it falls was simulated and further verified by Anderson [2] and his simulation of this is shown in Figure 6.1. For the glycol droplet-seeded air column case, however, the density does not reduce as drastically simply due to the fact that the column itself is ever so slightly heavier than the surrounding air and the mechanism in which the vorticity is deposited is not the same (see Section 2.7). Therefore, this phenomenon is only characteristic of the classical Richtmyer-Meshkov instability and not of the newly discovered Particle Lag instability.

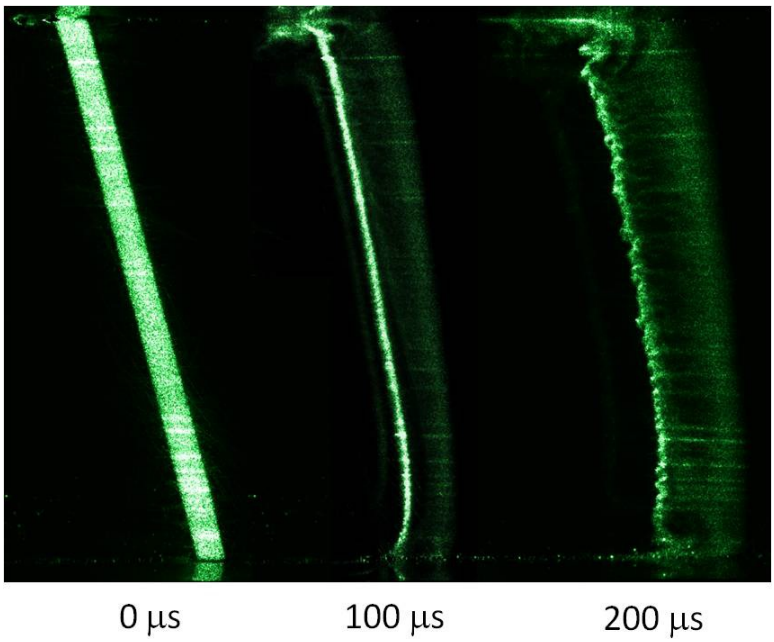

Figure 6.2: Side view of the glycol droplet-seeded SF_6 column at early times [2].

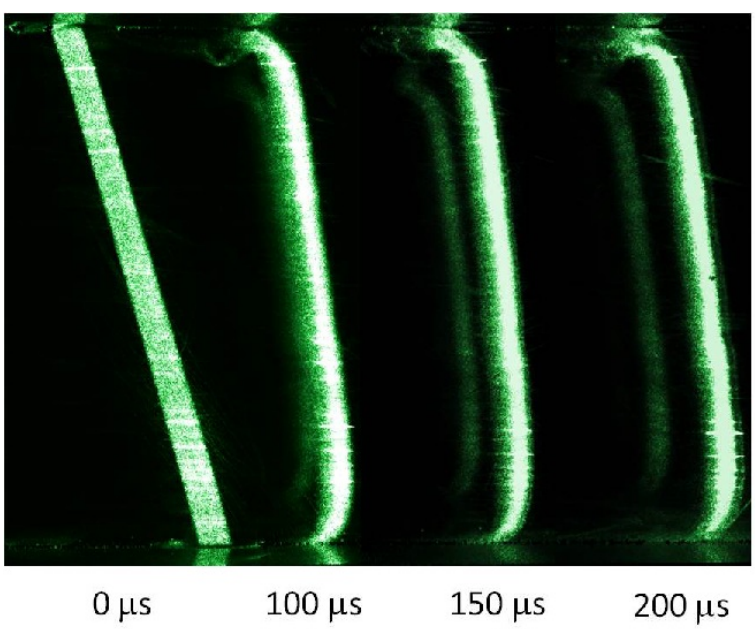

Figure 6.3: Side view of the glycol droplet-seeded air column at early times [2].

6.2 Secondary Instability Development

Another characteristic observed from these side views was the formation of smaller scale structures lining the entirety of the upstream side of the column. This is more clearly observed in the glycol droplet-seeded SF_6 column case. These small scale structures are the result of formation of secondary instabilities, which will eventually lead to turbulence. Among these secondary instabilities are the shear-driven Kelvin-Helmholz instability and the secondary baroclinic instability. The latter develops after the shock passage. The large-scale vortex cores are zones of low pressure, and the air and SF_6 are advected into them, resulting in pressure-density gradient misalignment.

6.3 Effects of Injection Holes

The diameter of our gas column is approximately 6 mm whereas the diameter of the hole in which the co-flow enters(see Section 3.2) is 12.7 mm. As the shock wave passes over the holes it is allowed to freely expand in the direction perpendicular to the shock (or streamwise) direction, directly affecting the development of the instabilities, especially near the bounding walls. This phenomenon is observed in the planar shock wave experiments as well [1, 2, 28] but is magnified significantly in the oblique orientation. In the planar experiments, much greater top-to-bottom symmetry was observed [1]. When the shock wave passes over the holes in the planar shock wave orientation, it experiences the *same* sharp corners on both the top and bottom injection holes. In the oblique orientation, the shape of the corners on the top and bottom of the test section are different: the top corner is an oblique angle, whereas the bottom corner is an acute angle. Figure 6.4 shows these differences. In combination with the density gradient effects, these corners affect the flow significantly. In

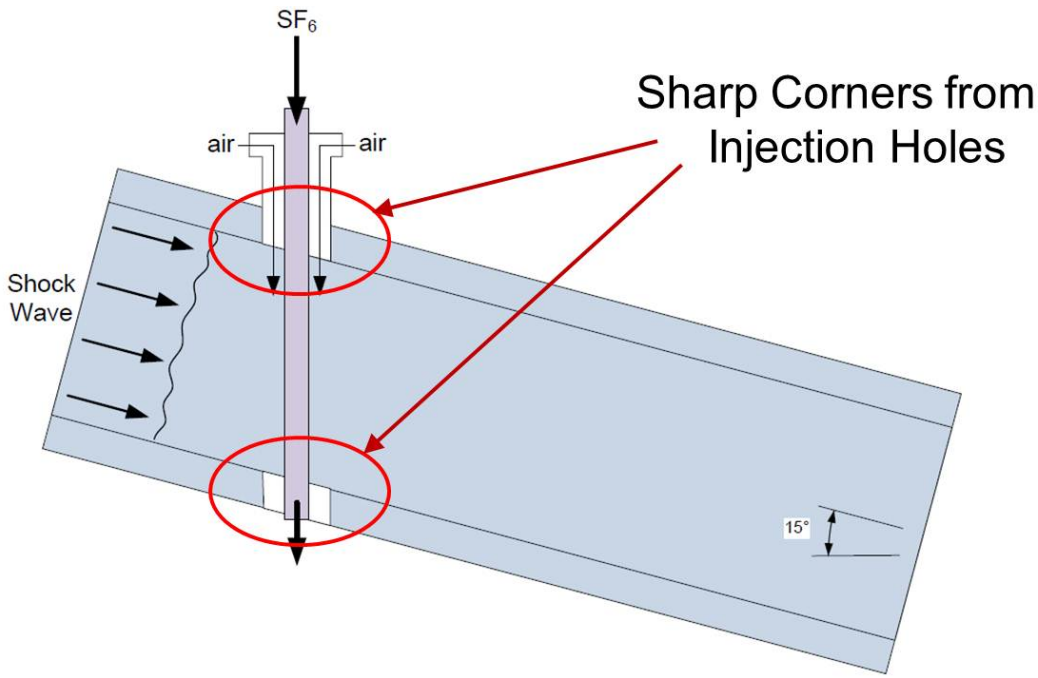

Figure 6.4: Schematic showing the sharp corners of the injection holes.

the plane 2 mm from the top boundary, the streamwise size of the perturbed cylinder is much larger than in other planes (Figures 5.4 and 5.7). Much of the material of the gas column gets entrained near the top boundary and a long tail develops, with the material staying very close to the boundary even into late times. This affects both gas column mixture but the effects of the injection holes is much more apparent in the glycol droplet-seeded SF_6 column case but further investigation into this mechanism is needed. Figure 6.5 demonstrates the large effect of the injection holes on the morphology of the instability. The effects are more prominent in the glycol droplet-seeded SF_6 column case.

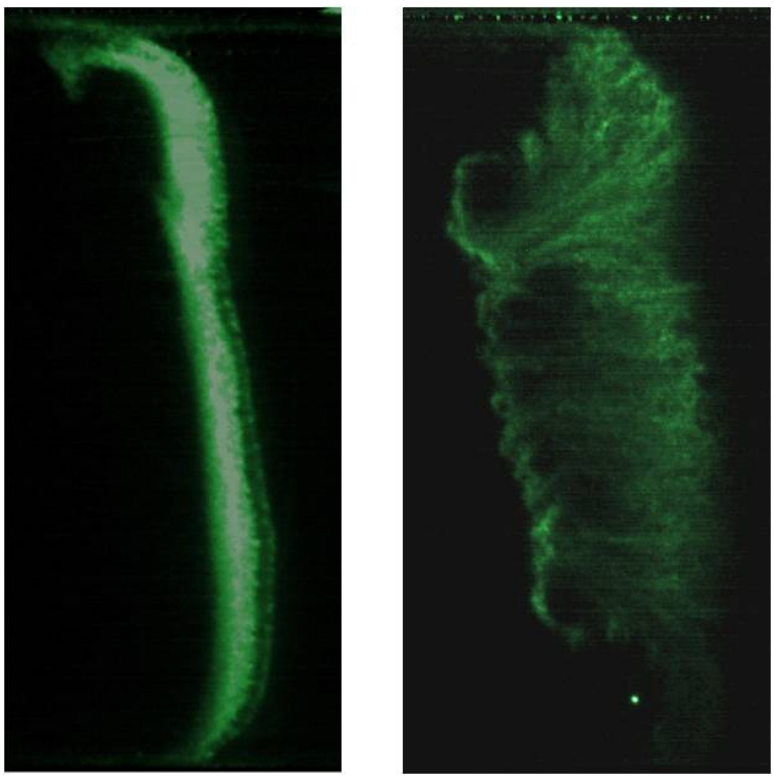

Figure 6.5: Side view of the glycol droplet-seeded air column (left) and the glycol droplet-seeded SF_6 column (right) at late times, roughly 650 μs after shock passage. The image extends the full height of the shock tube, i.e. 75 mm. [2]

6.4 Rotation of Gas Column

An investigation of how the gas column rotates was also performed. It was observed that the column underwent some straightening after the passage of the shock. Using the angle tool in ImageJ [33], several measurements of how much the column rotated were taken. Figure 6.6 demonstrates how the angle tool in ImageJ is used.

Measurements were taken for both the glycol droplet-seeded SF_6 column mixture and the glycol droplet-seeded air column mixture. The measurements are presented in Figure 6.7. The initial angle of the column varied from $15° \pm 0.5°$. This was be-

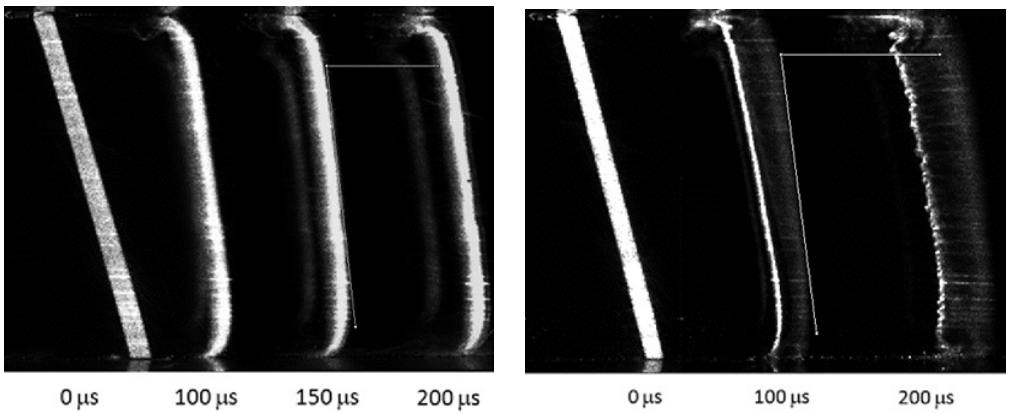

Figure 6.6: Schematic showing how the angle tool in ImageJ is used. The image on the left side is the glycol droplet-seeded air column mixture and the image on the right side is the glycol droplet-seeded SF_6 column mixture.

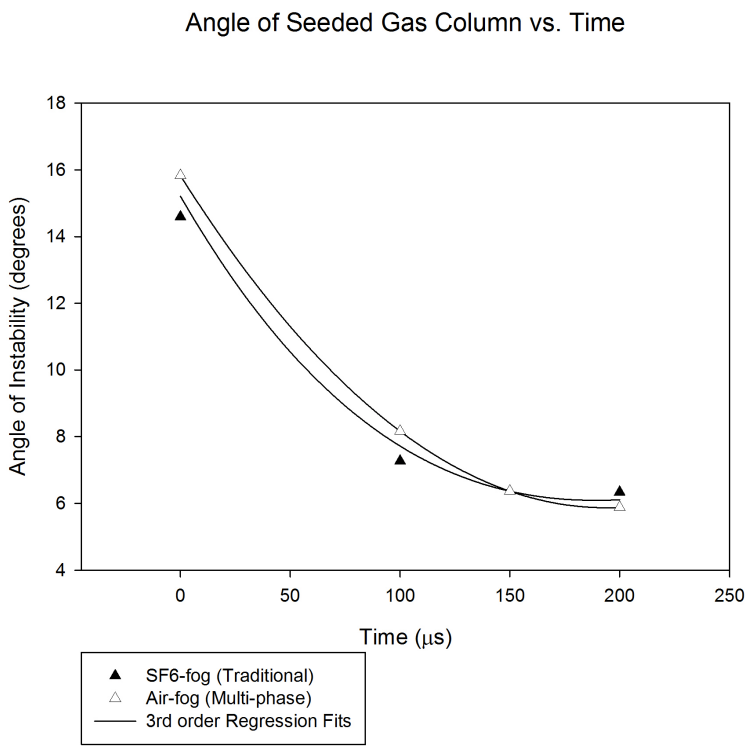

Figure 6.7: Graph showing the angle of the column (with respect to the vertical) vs time.

cause the gas column itself is only 5 mm in diameter whereas the exit hole is 11 mm in diameter, which allows for the column to move side-to-side slightly. From Figure 6.7 it can be seen that the rotation of the column stops shortly after shock acceleration. Also, there is no difference between the classical RMI and PLI, suggesting that the apparent rotation is mostly due to post-shock compression.

Chapter 7

Conclusions

This thesis presents experimental results for fluid instabilities generated by shock acceleration of a cylindrical column of gas seeded with glycol droplets. The work was performed at the University of New Mexico tiltable shock tube facility. The experimental images were obtained using planar laser visualization techniques in six different planes (five of which were oriented 15° from the horizontal along the shock tube, one of which was vertically oriented along the shock tube). Two cases were examined. The first was the classical Richymyer-Meshkov Instability (RMI), where the passing shock wave accelerated a column of sulfur-hexafluoride (SF_6) seeded with glycol droplets. The second, Particle Lag Instability (PLI), was a multi-phase analog to RMI where the passing shock wave accelerated a column of air seeded with glycol droplets. The mechanism via which vorticity is deposited differs from that of classical RMI in that there is no macroscopic density gradient between the gas column and the surrounding air.

An investigation of the three-dimensionality of the flow was performed. It was found that the effects of the injection holes significantly affect the flow characteristics, especially for the classical RMI case. The rotation of the gas column was found

to be independent of the gas being accelerated, suggesting rotation being mostly due to post-shock compression. Along with the simulations of Anderson [2], these experiments were used to validate some of his numerical data results and shed new light on the differences between planar and oblique shock wave interactions with gas column cylinders.

7.1 Future Work

In the future, a further look into the mechanisms in which an oblique shock wave interacts with a gas column should be considered. Increasing the tilt of the shock tube and performing some of the same studies should demonstrate similar results, although it would be expected that the effects of the injection holes would be greater. The rotation should asymptote to the approximate compression ratio just as presented here. In addition, more shear might be deposited on the upstream side of the fluid-fluid interface due to the fact that a larger portion of the shock velocity vector will be parallel with the axis of the gas column itself. Finally, a Mach number study should be performed to study on the compression ratio effects.

References

[1] P. Vorobieff et al., Physical Review Letters 106:184503 (2011).

[2] M. Anderson, Ph.D. Dissertation, The University of New Mexico (2011).

[3] S. Ukai, Master's Thesis, Georgia Institue of Technology (2010).

[4] H. Helmholtz, Monthly Reports of the Royal Prussian Academy of Philosophy in Berlin, 23:215-228 (1868).

[5] W. Thomson (Lord Kelvin), Philosophical Magazine 42:362-377 (1871).

[6] W. Broad, New York Times, (April 19, 2010).

[7] J.W. (Lord Rayleigh) Strutt, Proceedings of the London Mathematical Society S1-14.1:170-77 (1882).

[8] G.I. Taylor, Proceedings of the Royal Society of London, Series A, Mathematical and Physical Sciences 201 (1065):192-196 (1950).

[9] R. D. Richtmyer, Communications on Pure and Applied Mathematics 13:297-319 (1960).

[10] E. E. Meshkov, Soviet Fluid Dynamics 4:101-104 (1969).

[11] B. D.Collins et al., Journal of Fluid Mechanics, 464 (2002).

[12] K.O. Mikaelian, Physics of Fluids 6:1943 (1994).

[13] J. Kane et al., The Astrophysical Journal 511.1:335-40 (1999).

[14] R.D. Zucker et al., Fundamentals of Gas Dynamics, 2nd edition, Chapter 6 (2002).

[15] B.J. Balakumar et al., Physics of Fluids 20:124103 (2008).

[16] P. Vorobieff et al., Recent Research Developments in Fluid Dynamics, Volume 5:33-55 (2004).

[17] S. Elghobashi, Applied Scientific Research 48.3-4:301-14 (1991).

[18] J. McFarland et al., Physical Review Letters E84.2 (2011).

[19] X. Yang et al., Physics of Fluids A: Fluid Dynamics 4.7:1531 (1992).

[20] L. F. Henderson, Journal of Fluid Mechanics 198.1:365 (1989).

[21] J.F. Hawley, Physical Review Letters 63.12:1241-244 (1989).

[22] P. Colella et al., Journal of Computational Physics 54.1:174-201 (1984).

[23] R. Samtaney et al., Physics of Fluids A: Fluid Dynamics 5.6:1285 (1993).

[24] A. Palekar et al., Progress in Computational Fluid Dynamics, An International Journal 7.8:427 (2007).

[25] J.W. Jacobs, Journal of Fluid Mechanics 234.-1:629 (1992).

[26] C. Tomkins et al., Journal of Fluid Mechanics 611 (2008).

[27] E. Johnson, M.S. Thesis, The University of New Mexico (2009).

[28] J.E. Conroy, M.S. Thesis,The University of New Mexico (2012).

[29] G. C. Orlicz et al., Physics of Fluids 21, 064102 (2009).

[30] http://www.samwoosc.co.kr/pdf/new-wave/PV-GEM-DSa4-0312.pdf

[31] http://www.ansys.com/Products/Simulation+Technology/...
...Fluid+Dynamics/ANSYS+Fluent

[32] http://sine.ni.com/nips/cds/view/p/lang/en/nid/12638

[33] http://rsbweb.nih.gov/ij/